energies

MDPI

Article

Normalized-Characteristic-Current-Based Methodology for Quantifying Active Winding Reconfiguration Benefits in Permanent Magnet Synchronous Machines

Rajesh Kallur-Krishnamoorthy *, Haoran Wang, Hassan Currimbhoy, Markus Eisenbarth and Jakob Andert *

Chair of Mechatronics in Mobile Propulsion, Faculty of Mechanical Engineering, RWTH Aachen University, 52062 Aachen, Germany; wang_h@mmp.rwth-aachen.de (H.W.)
* Correspondence: kallur@mmp.rwth-aachen.de (R.K.-K.); andert@mmp.rwth-aachen.de (J.A.)

Abstract

Traction electric machines in electrified mobility are constrained by limited supply voltage and critical materials. Active winding reconfiguration (AWR) changes the winding connection during operation to improve voltage utilization and field-weakening (FW) capability. However, general design rules for AWR remain limited. This work extends the characteristic-current-based normalized parameter-plane framework to AWR via topology-dependent reconfiguration factors and evaluates the resulting torque-speed-power behavior over the design space. The analytical model is compared against finite-element analysis of six baseline machines and test-bench measurements from one machine. Normalized characteristic current is the dominant design parameter, capturing the balance between magnetic and current loading, while saliency and the reconfiguration factor set the magnitude of the benefit. Figures of merit are defined to quantify reconfiguration benefit across peak performance, crossover points, torque-speed envelopes, and part-load performance. Across these figures of merit, three explicit thresholds for normalized characteristic current are analytically derived and identified. Below the lowest threshold, designs such as synchronous reluctance and ferrite-assisted machines gain up to four times higher constant power speed range and 40% higher peak power, based on the analytical model. Above it and up to the middle threshold, conventional rare-earth traction machines gain mainly in part-load efficiency instead. Above the highest threshold, narrow-FW designs gain mainly in speed-range extension. These thresholds provide generalized, geometry-independent early-stage AWR screening for traction machine concepts.

Keywords: active winding reconfiguration; normalized parameter plane; characteristic current; saliency; traction electric machine; field weakening; permanent magnet synchronous machine; star-delta; series-parallel; winding reconfiguration; open-end winding

Check for updates

Academic Editors: Natalia Radwan-Pragłowska, Tomasz Wegiel and Maciej Sułowicz

Received: 9 September 2026
Revised: 1 October 2026
Accepted: 6 October 2026
Published: 13 October 2026

Copyright: © 2026 by the authors. Licensee MDPI, Basel, Switzerland. This article is an open access article distributed under the terms and conditions of the Creative Commons Attribution (CC BY) license.

1. Introduction

Primary traction electric drives for electrified mobility must balance cost, sustainability, and high-speed performance under a fixed direct current (DC) link voltage constraint. Several rare-earth-free rotor solutions exist, including induction machines (IM), synchronous reluctance machines (SynRM), permanent magnet (PM)-assisted SynRMs (PMaSynRM), and externally excited synchronous machines (EESM). Each introduces varying trade-offs with torque density, efficiency, volume, or thermal margin for reduced

critical-material content. A general survey in [1] compares EESMs with permanent magnet synchronous machines (PMSMs) and highlights this trade-off at a broad level. Under common stator and inverter constraints [2] shows that thermally limited EESMs achieve lower performance than neodymium–iron–boron (NdFeB)-PMSMs. Extending the comparison to ferrite-magnet PMaSynRMs and induction machines, ref. [3] shows that both are limited to about two-thirds of the best-case NdFeB-PMSM performance. When machine volume is not constrained, ref. [4] shows that ferrite-magnet PMaSynRMs require about 50% larger machine volume and 37% higher inverter current rating to match rare-earth machine performance.

Active winding reconfiguration (AWR) has regained attention as a means to address this trade-off. Early traction PMSM studies in [5] introduced star (Y), delta (Δ), and parallel (Π) reconfiguration using thyristors and electromechanical contactors. Tapped-winding layout using two three-phase diode bridges and two insulated-gate bipolar transistor (IGBT) switches were introduced in [6], including an unequally split tapped-winding topology [7], while ref. [8] proposed a combined tapped and Y–Δ topology for agricultural tractor application with a symmetric torque-interrupted switching sequence. More recently, ref. [9] applied an AWR series-parallel (Y–Π) topology to a ferrite-PMaSynRM. For induction machines, ref. [10] determined AWR for a single phase machine can provide three times speed extension, while ref. [11] applied Y–Π AWR to demonstrate three times increased power at extended speed range, whereas, a variable stator pole machine topology was proposed in [12]. A modeling method using winding function approach for the analysis of transient winding reconfiguration was proposed in [13]. Y–Π concepts with anti-parallel thyristor modules were studied in [14]. In [9], an AWR Y–Π topology was applied to a rotating 80 kW machine, but reconfiguration was limited to low speed and low torque because of high current transients. By contrast, ref. [15] demonstrated Y–Π AWR at moderate speed and torque representative of an automotive traction machine. While these studies addressed low-level reconfiguration switching using symmetric winding states during transition, asymmetric switching states were examined in [16] to minimize torque interruption, while ref. [17] considered similar sequencing for smaller machines. Ref. [18] proposed a fast reconfiguration control method for Y–Π switching within a single inverter switching period. The design proposed in [19] additionally discussed a fail-safe transition sequence using active short circuit during switching. Thus, several works have dealt with the wide ranging aspects around AWR design and control, and show the performance impact of the proposed design in terms of speed, torque, power and losses improvement. However, they remain largely at the level of single-point design demonstrations.

Reported gains in several of these studies are substantial and span a wide-range, including 20% to 80% increases in torque or power density and up to 60% reductions in total losses [20]. Yet, there is a lack of clear design parameters or threshold ranges to predict this benefit without a full design study. A sensitivity analysis [21] found that designs with weak rotor magnetic loading benefit more from AWR, albeit based on a single rotor design. However, the trend begins to reverse at very low magnetic loading and therefore does not generalize further. This work and a comprehensive review [20] identified the need for research on design methodologies for machines with reconfigurable windings from the conceptual stage. Identifying benefits currently requires a full AWR design study. Conventional multi-objective optimization methods require numerous detail design evaluations [22]. While data-driven approaches reduce this evaluation count [23,24], such design studies benefit from analytical methods to further reduce computational effort.

Generalized design-space explorations have used analytical normalized parameter-plane (NPP) models based on the flux-linkage–saliency ($\Psi_{PM} - \xi$) parameter-plane introduced in [25]. Practical saturation effects on the analytical model were examined in [26],

where constant power speed range (CPSR) predictions deviated by up to 69% for SynRMs, whereas surface PMSMs showed a deviation of about 7% when the parameters were obtained from an unsaturated state. This was further supported using results from finite-element-analysis (FEA) for an interior-PMSM (IPMSM) in [27], which showed saturation-induced CPSR deviations of roughly 47–54%, depending on the chosen parameters. Works in [28] applied $\Psi_{PM} - \xi$ NPP model to AWR at selected points. In [29], this $\Psi_{PM} - \xi$ NPP approach was extended to winding reconfiguration across the parameter plane, using a turns-ratio factor to compare operating-range improvements and validated the model with FEA. Ref. [30] expanded this framework into a common model covering several topologies including phase-number changes up to nine phases, and pole changing, thereby showing that different reconfiguration options can be compared within one framework; analytical results indicated the possibility of nearly doubling the torque-speed area. A volume-optimization study in [31] then applied the extended parameter plane to co-optimize motor and inverter volume, showing up to 27% total volume reduction and confirming the analytical trends experimentally. However, the boundaries identified in the NPP vary along the input parameters, requiring iterative solving or look-up tables (LUTs) for each design [32], even if these remain less resource intensive than multiple FEA simulations.

In [33] the importance of characteristic current (I_{ch}) in strongly influencing CPSR under field-weakening (FW) is highlighted. Ref. [34] shows that, although positioning the I_{ch} close to the rated current maximizes FW capability, it does not improve high-speed efficiency. Ref. [35] builds on this to propose an design-optimization criterion for positioning the characteristic current to enhance high-speed efficiency region. The normalized characteristic current ($\hat{I_{\mathrm{ch}}}$)-based NPP model introduced in [36] expresses a design-independent, closed-form boundary at $\hat{I_{\mathrm{ch}}} = 1$. This threshold value represents theoretical infinite CPSR capability. Moreover, the work showed that saturation can cause large deviations of up to 50% in peak torque from the analytical prediction, while the CPSR and FW envelope exhibit only minor deviation. Since AWR benefit is fundamentally governed by FW capability, this type of NPP model is well suited for extension to AWR topologies, although ref. [36] did not originally address AWR.

One study [37] extended the $\hat{I_{\mathrm{ch}}}$ based NPP model to AWR by introducing a third parameter, normalized FW current, for series-parallel reconfiguration topology. However, the study omitted the effect of turns ratio on PM flux linkage, as otherwise expected [28,30]. The same single threshold from [36], $\hat{I_{\mathrm{ch}}} = 1$, is identified qualitatively, without any figure of merit (FoM) to quantify torque or power gain over the CPSR. Validation is limited to a design at $\hat{I_{\mathrm{ch}}} = 4$, a machine with inherently narrow FW. The recommendation is that machines with narrow FW (large $\hat{I_{\mathrm{ch}}}$ and low saliency) primarily benefit from AWR and contradicts the findings in [21]. Broader case-study evidence [20] also indicate substantial AWR benefit for machines with wide FW and CPSR capability ($\hat{I_{\mathrm{ch}}} \approx 1$).

The gap therefore remains threefold: an AWR-extended $\hat{I_{\mathrm{ch}}}$ based NPP model that accounts for the turns-ratio effect on PM flux linkage, expression of reconfiguration benefit through quantified FoMs, and validation across the wide-FW region near $\hat{I_{\mathrm{ch}}} \approx 1$.

The goals of this work are:

1. Extend the two-parameter NPP model from [36] with turns-ratio effect to obtain a geometry-independent analytical model that predicts the torque-speed-power behavior of AWR topologies over the design space.
2. Derive a reduced set of FoMs from this model that quantify the benefit of AWR reconfiguration.
3. Identify explicit parameter thresholds that separate AWR-favorable from AWR-unfavorable design regions.

The remainder of this manuscript is organized as follows. Section 2 presents the analytical framework, AWR topologies, FoM definitions, and validation setup. Section 3 reports the model results and compares the analytical predictions with FEA and measurements. Section 4 interprets the main findings, limitations and derives design implications. Finally, Section 5 summarizes the conclusions, and outlines future work.

2. Materials and Methods

2.1. AWR Topologies and Notation

Most conventional traction machines use a three-phase winding driven by a two-level voltage source inverter (VSI) with one end of the phases joined at a common neutral point, i.e., in a star (Y) configuration. Actively reconfiguring the windings from this state changes the voltage utilization and FW capability. The following topologies are considered in this work, as summarized in Table 1 and represented in Figure 1.

- Star (Y): The anchor (*anc*) configuration; the three phases are joined at a common neutral point, driven by a single inverter.
- Delta (Δ): The three phases form a closed triangular loop, requiring a minimum of five switches [20,38]. Relative to Y, this increases effective phase voltage by $\sqrt{3}$ and reduces effective phase current by $1/\sqrt{3}$.
- Parallel (Π): Each phase winding is reconnected from series to parallel, giving an effective turns ratio $k_t = 1/2$ relative to Y; current per parallel branch is halved while the induced voltage is unchanged. This typically requires nine switches [20].

Table 1. AWR topologies and normalized reconfiguration parameters used in this work.

Topology	Symbol	$\frac{U_{phase,rec}}{U_{phase,anc}}$ [a]	$\frac{I_{phase,rec}}{I_{phase,anc}}$	k_t	Switches
Star	Y	1	1	1	-
Delta	Δ	$\sqrt{3}$	$\frac{1}{\sqrt{3}}$	1	5
Parallel	Π	1	1	$\frac{1}{2}$	9

[a] Anchor configuration denoted by *anc*; reconfigured state denoted by *rec*. Voltage and current ratios are defined at the phase terminals — for parallel configuration, the phase current is unchanged, but the current density in each parallel branch is halved.

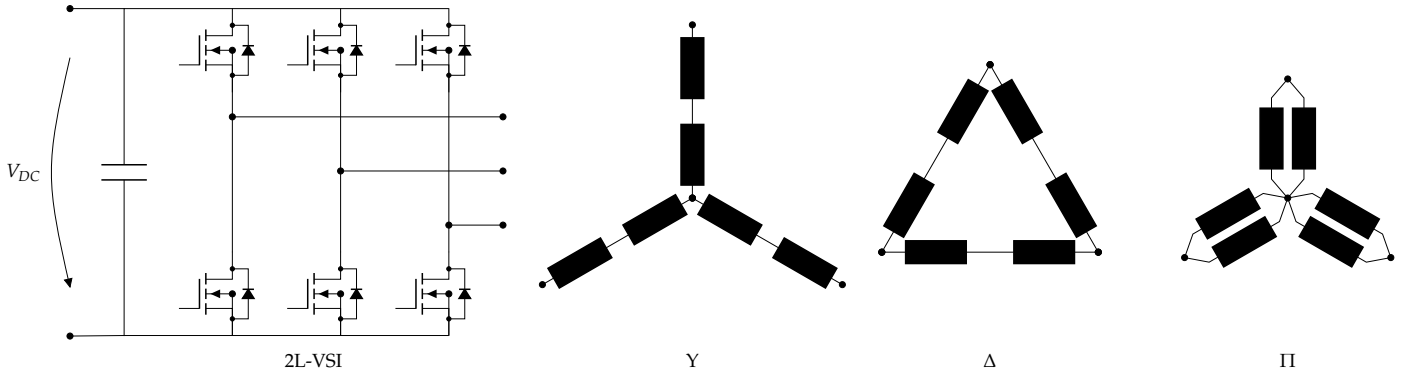


Figure 1. Machine winding topologies considered in this work connected to a two-level voltage source inverter.

2.2. NPP Model

Following standard assumptions apply to the simplified d-q model representation of IPMSM machines [25,30,36]:

1. Lossless machine: stator (phase) resistance and all loss terms (iron loss, friction, leakage etc.) are set to zero.
2. Fundamental-wave, sinusoidal operation: higher harmonics are neglected, and sinusoidal quantities are assumed.
3. No cross-coupling: cross-coupling is neglected. Ψ_d and Ψ_q are solely dependent on I_d and I_q, respectively.
4. Linear magnetic properties: saturation effects and temperature-dependent changes of PM flux are neglected.
5. Steady-state operation: time-derivative terms in the voltage equations are zero.
6. No temperature dependence: Temperature-dependent electromagnetic and resistive properties are neglected assuming equal thermal conditions.

2.2.1. Fundamentals of NPP Model Equations

The normalized voltage and torque equations, derived from the established absolute d-q model is described in [36], with normalization base quantities reproduced in Appendix A, as used in this work are:

$$\hat{U_d} = -\hat{\Psi_q}\hat{\omega_e} \tag{1}$$

$$\hat{U_q} = +\hat{\Psi_d}\hat{\omega_e} \tag{2}$$

$$\hat{\Psi_d} = \hat{L_d}\hat{I_d} + \hat{\Psi_{PM}} \tag{3}$$

$$\hat{\Psi_q} = \hat{L_q}\hat{I_q} \tag{4}$$

$$\hat{T_e} = \hat{\Psi_{PM}}\hat{I_q} + \left(\hat{L_d} - \hat{L_q}\right)\hat{I_d}\hat{I_q} \tag{5}$$

$$\hat{P} = \hat{T_e}\hat{\omega_e} \tag{6}$$

$$\hat{I_{lim}} = \sqrt{\hat{I_d}^2 + \hat{I_q}^2} \tag{7}$$

$$\hat{U_{lim}} = \sqrt{\hat{U_d}^2 + \hat{U_q}^2} \tag{8}$$

The voltage limit Equations (1)–(4) and (8), show an ellipse whose d- and q-axes diameters are inversely proportional to the product of machine speed $\hat{\omega_e}$ and the respective inductances, $\hat{L_d}$ and $\hat{L_q}$. The center of these ellipses is given by the characteristic current, $\hat{I_{ch}}$, and the ratio of the q- and d-axis inductances defines the saliency, ξ, of the machine.

$$\xi = \frac{\hat{L_q}}{\hat{L_d}} \tag{9}$$

$$\hat{I_{ch}} = -\frac{\hat{\Psi_{PM}}}{\hat{L_d}} \tag{10}$$

The normalization of any given reference drive and reference machine is made with the drive current and voltage limits set to one. The base speed of the reference machine, defined as the speed at which the voltage and current limits of the reference drive under maximum torque per ampere (MTPA) control are reached, is normalized to one. With this convention, the reference drive and machine transitions from current-limited operation to FW operation at this normalized speed value of one. This convention is consistent with standard parameter-plane formulations discussed in Section 1 and coincides with the method of normalization in [36].

2.2.2. Significance of Normalized Characteristic Current

Previous research established NPP models for describing the FW capability of IPMSM. In this work, the formulation based on normalized characteristic current $\hat{I_{ch}}$ and saliency ratio ξ is used. The characteristic current is a fundamental machine parameter and forms a

key boundary recognized for its role in determining FW performance. In its normalized form (i.e., $\hat{I_{ch}}$), values above one indicate that the voltage limit ellipse intersect is outside the current limit circle, so the machine becomes speed-limited, whereas values below one allow continued FW toward higher speed with diminishing torque. Saliency ξ modifies the shape of the voltage-limit ellipse and therefore the effectiveness of current utilization in FW; higher saliency reduces the d-axis current needed to remain within the voltage limit and improves torque-per-ampere output.

The characteristic current represents the ratio of the magnet flux to the d-axis inductance. When normalized against maximum stator current limit, it points to the machine's relative magnetic loading and current loading, both fundamental design parameters in preliminary, analytical machine design.

The characteristic current also equals the balanced three-phase steady-state short-circuit current of the machine at high-speeds under idealized assumptions. $\hat{I_{ch}}$ placed near the maximum current limit therefore implies that a stator short circuit alone can approach the magnet's demagnetizing field. Reduced- and rare-earth-free magnet designs, with lower demagnetization resistance, thus often target $\hat{I_{ch}}$ below this limit, most notably in ferrite PMaSynRM. $\hat{I_{ch}}$ thus also captures the trade-off between demagnetization resistance and FW capability.

Together, $\hat{I_{ch}}$ and ξ provide a physically grounded way to locate traction-machine designs in the NPP. In this plane, most wide-CPSR machines, including those in automotive traction use, typically occupy the region with characteristic current around the rated maximum current limit (i.e., $0.8 < \hat{I_{ch}} < 1.2$) and a saliency, $\xi > 1$ [34].

2.3. Extension of the $\hat{I_{ch}}$–ξ NPP Model to AWR

The equivalent effect of winding reconfiguration on the voltage, current and torque equations is represented by a factor, $k_{w,rec}$. The anchor state (*anc*) is the Y configuration, and the reconfigured states (*rec*) are the Δ and Π configurations.

The peak phase MMF ($\mathcal{F}$) of the anchor configuration is defined as:

$$\hat{\mathcal{F}}_{anc} = N_t \cdot \hat{I_{lim}} \tag{11}$$

where N_t is the number of series turns per phase and $\hat{I_{lim}}$ is the normalized current limit.

The peak phase MMF ($\hat{\mathcal{F}}$) of the reconfigured state is then defined as:

$$\hat{\mathcal{F}}_{rec} = \frac{\hat{\mathcal{F}}_{anc}}{k_{w,rec}} \tag{12}$$

The turns-ratio also affects the flux linkage and the inductances. The underlying reluctance and the PM flux remain unchanged, but the effect of the turns ratio appears in the flux linkage and in the inductance: the flux linkage scales proportionally with the turns ratio, while the inductance scales quadratically [28,30,38].

$$k_t = \frac{N_{t,rec}}{N_{t,anc}} \tag{13}$$

$$\Psi_{PM,rec} = k_t \cdot \Psi_{PM,anc} \tag{14}$$

$$L_{d,rec} = k_t^2 \cdot L_{d,anc} \tag{15}$$

$$L_{q,rec} = k_t^2 \cdot L_{q,anc} \tag{16}$$

For any configuration, the onset of FW is the point at which the induced voltage reaches the voltage limit. The reconfiguration factor can be used to relate the voltage limit of the reconfigured state to that of the anchor state as follows:

$$\hat{U}_{\mathrm{ind,max}} = \hat{U_{\mathrm{lim}}} \tag{17}$$

$$\hat{U}_{\mathrm{lim},\Delta} = k_{\mathrm{w,rec},\Delta} \cdot \hat{U}_{\mathrm{lim,Y}} \tag{18}$$

$$\hat{U}_{\mathrm{ind,max},\Pi} = k_{\mathrm{w,rec},\Pi} \cdot \hat{U}_{\mathrm{ind,max,Y}} \tag{19}$$

For the Δ configuration, $k_{\mathrm{w,rec}}$ is the ratio of the current and voltage limits between line and phase quantities. For the Π configuration, $k_{\mathrm{w,rec}}$ is the inverse of the turns-ratio between the reconfigured and anchor windings. The flux linkage, inductances, the voltage- and current-limits collectively make up the torque-speed Equations (1)–(8). Thus, the $k_{\mathrm{w,rec}}$ factor is incorporated into those equations using these relationships, as summarized in Table 2.

Table 2. Normalized model parameters for the AWR configurations.

Parameter	Y	Δ	Π	Remark
$k_{\mathrm{w,rec}}$	1.0	$\sqrt{3}$	2.0	Reconfiguration factor
$\hat{I_{\mathrm{lim}}}$	1.0	$\frac{1}{k_{\mathrm{w,rec}}}$	1.0	Normalized current limit
$\hat{U_{\mathrm{lim}}}$	1.0	$k_{\mathrm{w,rec}}$	1.0	Normalized voltage limit
k_{t}	1	1	$\frac{1}{k_{\mathrm{w,rec}}}$	Turns per phase ratio

Analysis is then carried out pointwise in the $(\hat{I_{\mathrm{ch}}}, \xi)$ plane. Each point representing the parameter pair defines an anchor machine in the Y configuration. For each anchor machine, the AWR topologies defined in Section 2.1 are evaluated as alternative reconfigured operating states of the underlying anchor machine by applying topology-dependent changes in current limit, voltage limit, or effective turns per phase, as summarized in the Table 2. This interpretation reflects the physical premise of AWR: the winding connection is reconfigured during operation whereas the machine geometry and material system remain unchanged.

The normalization established for the Y configuration remains applicable across all reconfigured states. Thus, keeping a normalized circle diagram from the Y configuration as the anchoring reference, MTPA and Maximum torque per voltage (MTPV) loci are generated for each topology, along with the resulting torque–speed envelopes, following the methodology in [36]. The corner-speed of the anchoring Y configuration always appears at the normalized value of unity, whereas the corner-speed of the reconfigured topologies appears at different normalized values.

All configurations are compared at the same inverter line current and voltage limits; for the Π configuration the current density in each parallel branch is halved (see note: Table 1) which is the equivalent of halving the total turns in series per phase. For the Δ configuration the phase current limit is reduced by $\sqrt{3}$, as shown in Table 2.

The resulting comparison at each point in the parameter plane represents the effect of reconfiguration on one underlying machine design. This avoids renormalization per topology and ensures that all the corresponding torque–speed envelopes of the underlying machine design are directly comparable.

The comparison of torque–speed envelopes at selected $\hat{I_{\mathrm{ch}}}$–ξ value pairs (Figure 2) provides only a preliminary view of the effect of reconfiguration. In a subsequent section, scalar FoM are defined to systematically identify beneficial design regions across the entire parameter plane and to facilitate machine-level benchmarking.

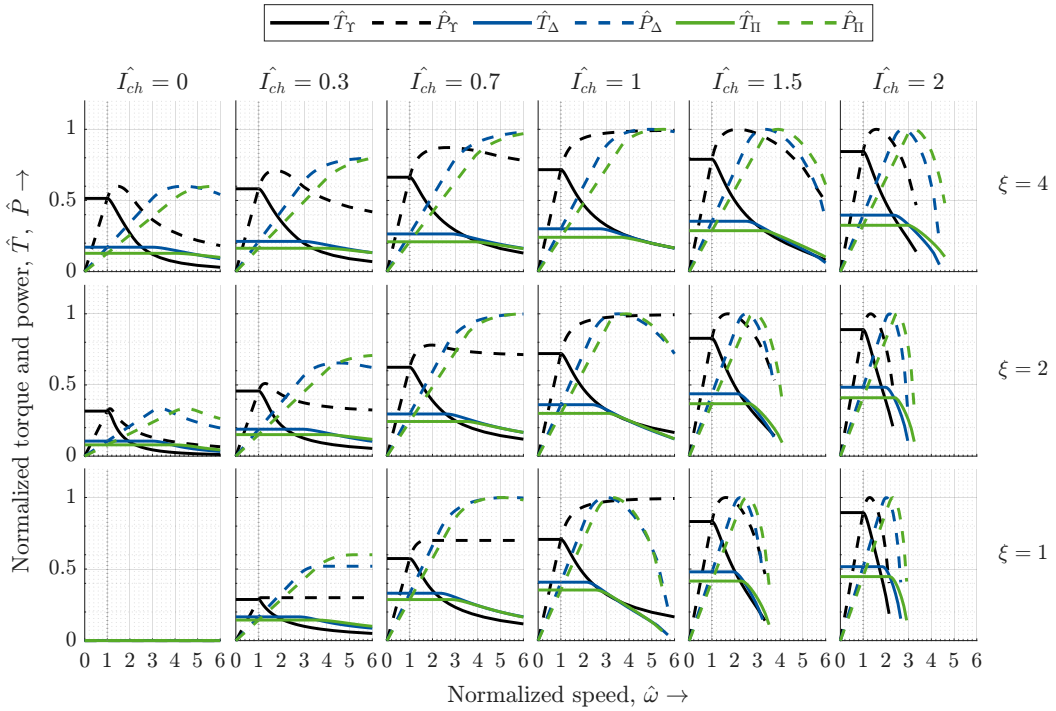


Figure 2. Selected value pairs from the $(\hat{I_{\text{ch}}}, \xi)$ parameter plane, with corresponding torque-speed envelopes for the anchor and reconfigured topologies.

2.4. CPSR Potential Speed Ratio and Threshold Values for $\hat{I}_{\text{ch}}$

Under the assumptions of the NPP model, a ratio is defined called the CPSR potential speeds ratio of the reconfigured and anchor states, and is given by:

$$r_\omega = \left| \frac{\omega_{0,\text{rec}}}{\omega_{0,\text{anc}}} \right| = \left| \frac{k_{\text{w,rec}}(\hat{I}_{\text{ch}} - 1)}{\hat{I}_{\text{ch}} - \frac{1}{k_{\text{w,rec}}}} \right| \tag{20}$$

The behaviour of this ratio is shown in Figure 3. It is independent of saliency, ξ, and valid for the normalization framework used in this study.

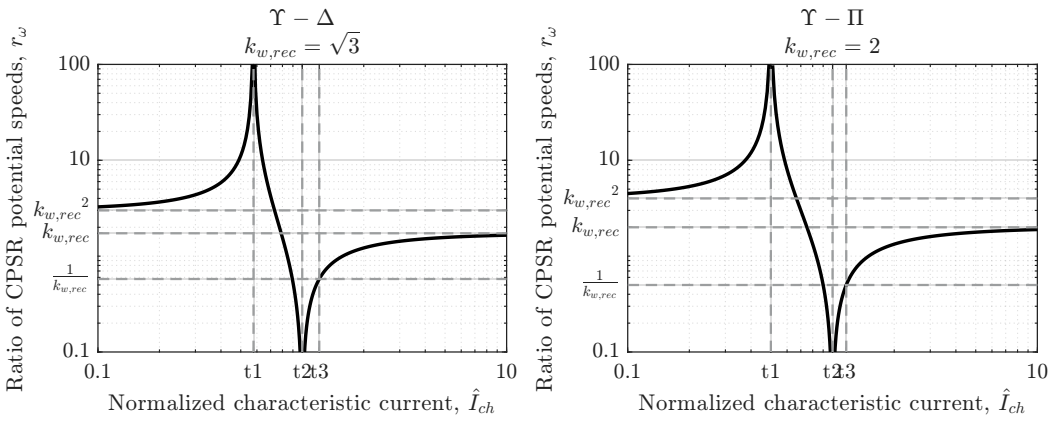


Figure 3. Behaviour of ratio of CPSR potential speeds r_ω as a function of $\hat{I_{\text{ch}}}$. Dashed lines highlight important thresholds of r_ω and $\hat{I_{\text{ch}}}$.

From this ratio, three threshold values are obtained. The first threshold is the point where the reconfigured state has a theoretical infinte CPSR, so that $r_\omega \to \infty$, the envelope and the resulting benefits are maximized. Solving for the anchor-referenced characteristic current gives,

$$t_1: \quad \hat{I}_{\text{ch}} = \frac{1}{k_{\text{w,rec}}} \tag{21}$$

The second threshold follows is the point where the anchor state has theoretically infinite CPSR, which corresponds to $r_\omega \to 0$. This means that the anchor state already has theoretically infinite CPSR, i.e., a maximal envelope and the reconfigured state cannot significantly improve the composite envelope. This gives

$$t_2: \quad \hat{I}_{\text{ch}} = 1 \tag{22}$$

Beyond t_2, the reconfigured and anchor CPSR potential speeds approach each other again. At the point where the CPSR potential speed of the anchor state is reconfiguration factor times the reconfigured state, the reconfigured state envelope starts showing potential to improve the composite envelope.

$$r_\omega = \frac{1}{k_{\text{w,rec}}} \tag{23}$$

Solving this condition gives

$$t_3: \quad \hat{I}_{\text{ch}} = \frac{k_{\text{w,rec}}^3 - 1}{k_{\text{w,rec}}(k_{\text{w,rec}}^2 - 1)} = 1 + \frac{1}{k_{\text{w,rec}}(k_{\text{w,rec}} + 1)} \tag{24}$$

Thresholds t_2 coincides with [36]. Threshold t_1 and t_3 are direct results of $k_{w,rec}$ from this study. Whereas threshold t_2 holds additional meaning based on the implication for the reconfigured state with $k_{w,rec}$. The derivation of the CPSR potential speed ratio and the $\hat{I}_{\text{ch}}$ threshold values is provided in Appendix B.

Note: The threshold values above are ideal values from the ideal lossless, linear assumptions. Upon considering resistance and saturation, the analytical solution of the thresholds are offset by:

$$t_{n,non-ideal} = t_{n,\text{ideal}} + \frac{\hat{R}}{\hat{L}_d}, \quad n \in \{1,2,3\} \tag{25}$$

2.5. FoM for Evaluating Reconfiguration Benefit

FoMs are defined to systematically identify behavior around thresholds and derive implication for design-rules across the parameter plane.

A summary of the different FoMs are given in Tables 3 and 4, while Figure 4 illustrates the reference points used in their definitions. The FoMs are primarily grouped in to four types.

1. Maximum performance
2. Crossover point
3. CPSR and FW range
4. Part-load performance

Table 3. Definitions used in the derivation of FoMs.

Helper	Symbol	Equation	Physical Meaning/Design Relevance
Torque difference	$\Delta\hat{T}(\hat{\omega})$	$= \Delta\hat{T}(\hat{\omega}) = \hat{T}_{\text{rec}}(\hat{\omega}) - \hat{T}_{\text{anc}}(\hat{\omega})$	Pointwise torque difference used to locate the first crossover speed.
Common valid speed interval	Ω_{c}	$= [0, \min(\hat{\omega}_{\text{end,anc}}, \hat{\omega}_{\text{end,rec}})]$	Shared speed range over which anchor and reconfigured envelopes are compared.
Composite envelope torque	$\hat{T}_{\text{env}}(\hat{\omega})$	$= \max(\hat{T}_{\text{anc}}(\hat{\omega}), \hat{T}_{\text{rec}}(\hat{\omega}))$	Point-wise composite torque envelope used in the area-ratio definition.

Table 3. *Cont.*

Helper	Symbol	Equation	Physical Meaning/Design Relevance
CPSR threshold speed	$\hat{\omega}_{e,\mathrm{CPSR}}$	$= \max\left\{\hat{\omega}_e \in [\hat{\omega}_{e,c}, \hat{\omega}_{e,\mathrm{end}}] \mid \hat{P}(\hat{\omega}_e) \geq \hat{P}_c\right\}$	Speed at which constant-power operation ends for a given torque level.
Rated CPSR power	$\hat{P}_c$	$= \hat{T}_c \hat{\omega}_{e,c}$	Constant-power threshold fixed at the corner point. For the composite envelope, the first corner point of the combined envelope is the consistent reference across the parameter plane.
Composite power envelope	$\hat{P}_{\mathrm{env}}(\hat{\omega})$	$= \max\left(\hat{P}_{\mathrm{anc}}(\hat{\omega}), \hat{P}_{\mathrm{rec}}(\hat{\omega})\right)$	Pointwise power envelope used to compute composite CPSR.
Common operating area	A_{c}	$= \iint_{\Omega_{\mathrm{c}}} \mathrm{d}\hat{\omega}\, \mathrm{d}\hat{T}$	Intersection of feasible operating areas of both configurations.

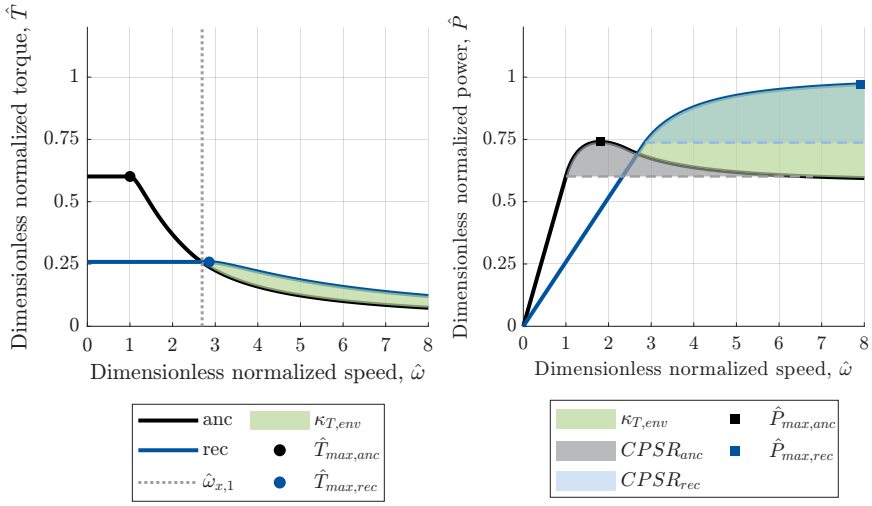


Figure 4. Exemplary torque-speed envelopes of anchor and reconfigured configurations, with the corresponding points of reference used in the definitions of FoMs in Table 4.

Table 4. FoMs used to quantify the benefit of reconfiguration.

FoM [a]	Symbol	Equation	Physical Meaning/Design Relevance
		Maximum performance FoMs	
Corner-point torque ratio	$\kappa_{T,c}$	$= \dfrac{\hat{T}_{\mathrm{rec}}(\hat{\omega}_{e,c,\mathrm{rec}})}{\hat{T}_{\mathrm{anc}}(\hat{\omega}_{e,c,\mathrm{anc}})}$	Base-speed torque ratio; values below unity indicate a torque penalty for reconfiguration.
Peak power ratio	$\kappa_{P,\max}$	$= \dfrac{\max_{\hat{\omega}\in\Omega} \hat{P}_{\mathrm{rec}}(\hat{\omega})}{\max_{\hat{\omega}\in\Omega} \hat{P}_{\mathrm{anc}}(\hat{\omega})}$	Ratio of absolute peak powers, (rec)/(anc); values above unity indicate a peak-power benefit.
		Crossover point FoMs	
First crossover speed	$\hat{\omega}_{x,1}$	$= \arg\min_{\hat{\omega}\in\Omega} \lvert\Delta\hat{T}(\hat{\omega})\rvert$	Speed at which the torque envelopes first crossover; lower values indicate earlier benefit from reconfiguration.
Crossover voltage-stress factor	$\kappa_{u,x,1}$	$= \hat{\omega}_{x,1} \cdot \hat{\Psi}_{\mathrm{PM}}$	Normalized induced voltage at the crossover speed; indicates voltage-stress and mode-shift risk.
		CPSR FoMs	
Composite AWR CPSR	$\kappa_{\mathrm{CPSR,env}}$	$= \dfrac{\hat{\omega}_{\mathrm{CPSR,env}}}{\hat{\omega}_{CPSR,\mathrm{anc}}}$	System-level CPSR gain of the reconfigured drive relative to the anchor drive.
Composite torque-area ratio	$\kappa_{T,\mathrm{env}}$	$= \dfrac{\int_{\hat{\omega}\in\Omega} \hat{T}_{\mathrm{env}}(\hat{\omega})\, \mathrm{d}\hat{\omega}}{\int_{\hat{\omega}\in\Omega} \hat{T}_{\mathrm{anc}}(\hat{\omega})\, \mathrm{d}\hat{\omega}}$	Fractional expansion of the torque–speed operating area over the common speed interval.

Table 4. *Cont.*

FoM [a]	Symbol	Equation	Physical Meaning/Design Relevance
		Part-load performance FoMs	
Mean PF improvement	$\bar{\kappa}_{PF}$	$= \frac{1}{A_c} \iint_{\Omega_c} [PF_{rec}(\hat{\omega}, \hat{T}) - PF_{anc}(\hat{\omega}, \hat{T})] \, d\hat{\omega} \, d\hat{T}$	Area-averaged PF gain over the common operating map.
Mean copper-loss improvement	$\bar{\kappa}_{Cu}$	$= \frac{1}{A_c} \iint_{\Omega_c} [\hat{P}_{Cu,anc}(\hat{\omega}, \hat{T}) - \hat{P}_{Cu,rec}(\hat{\omega}, \hat{T})] \, d\hat{\omega} \, d\hat{T}$	Area-averaged copper-loss reduction over the common operating map.

[a] All κ ratios are (rec)/(anc) (reconfigured over anchor) unless stated otherwise. Values above unity indicate an improvement relative to the anchor configuration. The subscript (env) denotes the composite envelope formed from the pointwise maximum of both configurations.

2.6. Baseline Traction-Machine Set and Finite-Element Models

The results from the analytical extended NPP model, and the FoMs derived from it, are evaluated using numerical models of representative automotive traction machines. Using detailed cross-sectional geometry, FEA models can provide sufficient fidelity in capturing nonlinear, saturation-dependent electromagnetic behavior across the full operational range. The evaluation is to quantify the correlation of important trends between the analytical model and the numerical models, and to identify any limitations of the analytical model. This section describes in brief the approach to FEA of the four representative automotive traction machines and two benchmark virtual designs of automotive traction machines (Table 5).

Table 5. Machine specifications for baseline machines M1–M6.

Parameter	M1	M2	M3 [b]	M4	M5 [c]	M6 [c]
Symbol [a]	●	■	★	▼	♦	▲
Rotor topology	IPMSM	IPMSM	IPMSM	IPMSM	PMaSynRM	PMaSynRM
Magnet material	NdFeB N30UH	NdFeB N38UH	NdFeB N38UH	NdFeB N48UH	Ferrite NMF-15G	Ferrite NMF-15G
Magnet layout [d]	▽	2∨	2∨	1∨	4∪	5∪
Lamination Material	NO27-1400H	NO25-1350H	NO25-1350H	NO27-1400H	NO27-1400H	NO27-1400H
Stator slots [e]	48	48	48	72	72	72
Pole-pairs [e]	4	4	4	3	3	3
System rated DC-link voltage in V	400	800	800	800	1200	1200
Nominal DC-link voltage [e] in V	350	650	650	650	1000	1000
Modulation index [e]	0.924	0.924	0.924	0.95	0.95	0.95
Maximum RMS line current [e] in A	600	230	180	530	280	280
Maximum mechanical torque in N m	310	350	342	455	387	391
Maximum mechanical power [f] in kW	170	155	100	250	192	169
Maximum rotational speed [e] in min^{-1}	16,000	17,000	17,000	20,000	15,000	15,000
Active parts outer diameter [e] in mm	220	200	200	234	234	234
Active length [e] in mm	175	156	156	130	130	130

[a] Used to represent the machines in Figures 6 and 7. [b] Machine M3 is an open-end winding machine used for measurement. [c] M1–M3, M4 are commercially available traction machines used as reference machines. M5 and M6 are virtual ferrite PMaSynRM benchmark designs derived from M4. [d] Magnet-layout symbols: ▽ denotes an inverse-delta layout; 1∨ and 2∨ denote single- and double-layer V-shaped layouts; 4∪ and 5∪ denote four- and five-layer U-shaped layouts. [e] Values used in FEA simulations. All machines use copper winding. [f] At nominal voltage and maximum RMS line current.

FEM Modeling

Electromagnetic modeling and FEA of the baseline machines is performed with the commercial software Ansys Motor-CAD (2025R1) [39] using its two-dimensional (2D) transient finite-element-method solver. The geometry of machines M1–M3 is reconstructed

after direct measurement from the machines' active parts. Whereas, the geometry and model parameters of M4–M6 are derived from manufacturer design data. The machines are radial flux machines. Transient 2D FEA model of the smallest symmetric machine sector is used with ideal balanced sinusoidal current excitation and constant rotor speed. End effects are handled separately, and materials are modeled as isotropic at a fixed uniform temperature of 318 K. Background information on the FEA modeling approach and the assumptions made in the modeling of the baseline machines are provided in Appendix D.

2.7. Measurement of Machine M3

Machine M3, the device under test (DUT) is an open-end winding machine that can be reconfigured between Y and Δ configurations. It was measured on a dynamometer test bench (Figure 5 and Table 6) to validate the FEA model and to provide experimental data for comparison with the analytical model. The machine was operated using field-oriented control, while the dynamometer imposed the speed setpoint. Manual reconfiguration between Y and Δ was performed using the terminal box shown in Figure 5. Shaft torque, shaft speed, three-phase line currents and voltages were recorded using the measurement equipment summarized in Appendix C. The experimental results are limited to the steady-state characteristics of machine M3 in the Y and Δ configurations, reconfigured manually via a terminal box. Switching transients and voltage stresses during reconfiguration were not experimentally investigated.

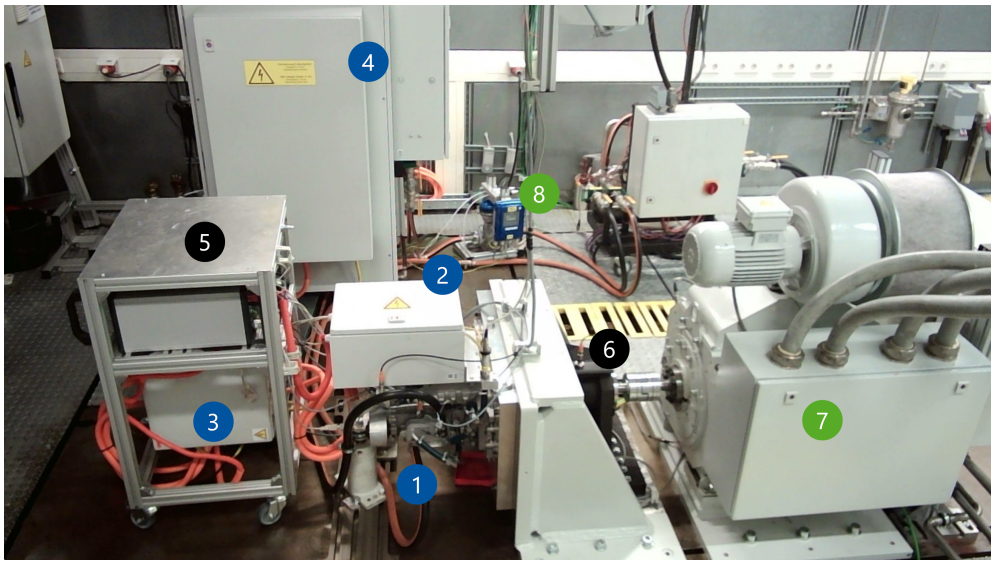


Figure 5. Dynamometer test bench for machine M3. Numbered components are listed in Table A3. Blue: DUT and associated high voltage power supply chain components. Black: Measurement sensors. Green: Dynamometer equipment.

Table 6. Numbered components of the dynamometer test bench for machine M3 shown in Figure 5.

No.	Component	No.	Component
1	Device under test	5	Electrical signal acquisition
2	Reconfiguration terminal box	6	Torque and speed measurement
3	Inverter terminal box and electrical sensor unit	7	Load machine
4	Inverter	8	Cooling system

3. Results

3.1. Maximum Performance FoMs

The inverse torque ratio in Figure 6 transitions between two limits. For $\xi = 1$, torque depends only on $\hat{I}_q$. Consequently, the inverse torque ratio equals $k_{w,rec}$. For $\hat{I_{ch}} = 0$, the

optimum occurs at $\hat{I}_{\mathrm{d}} = \hat{I}_{\mathrm{q}}$. As a result, torque becomes proportional to the square of the current magnitude and the inverse torque ratio becomes $k^2_{\mathrm{w,rec}}$.

Peak power and its FoM,$\kappa_{P,\mathrm{max}}$, in Figure 6 shows three distinct regions of behavior with respect to $\hat{I_{\mathrm{ch}}}$ and $k_{\mathrm{w,rec}}$:

- For $\hat{I_{\mathrm{ch}}} = 0$, reconfiguration only shifts the speed at which maximum power occurs, resulting in $\kappa_{P,\mathrm{max}} = 1$.
- For $\hat{I_{\mathrm{ch}}} \leq \frac{1}{k_{\mathrm{w,rec}}}$, the reconfigured state can raise maximum power, and $\kappa_{P,\mathrm{max}} \simeq k_{\mathrm{w,rec}}$ for $\xi = 1$. Machines with $\xi > 1$ show improvement of more than 40% in peak power.
- For $\hat{I_{\mathrm{ch}}} > \frac{1}{k_{\mathrm{w,rec}}}$, the benefit vanishes towards $\kappa_{P,\mathrm{max}} \leq 1$ at a threshold of $\hat{I_{\mathrm{ch}}} \simeq 1$, and stays below unity for higher $\hat{I_{\mathrm{ch}}}$.

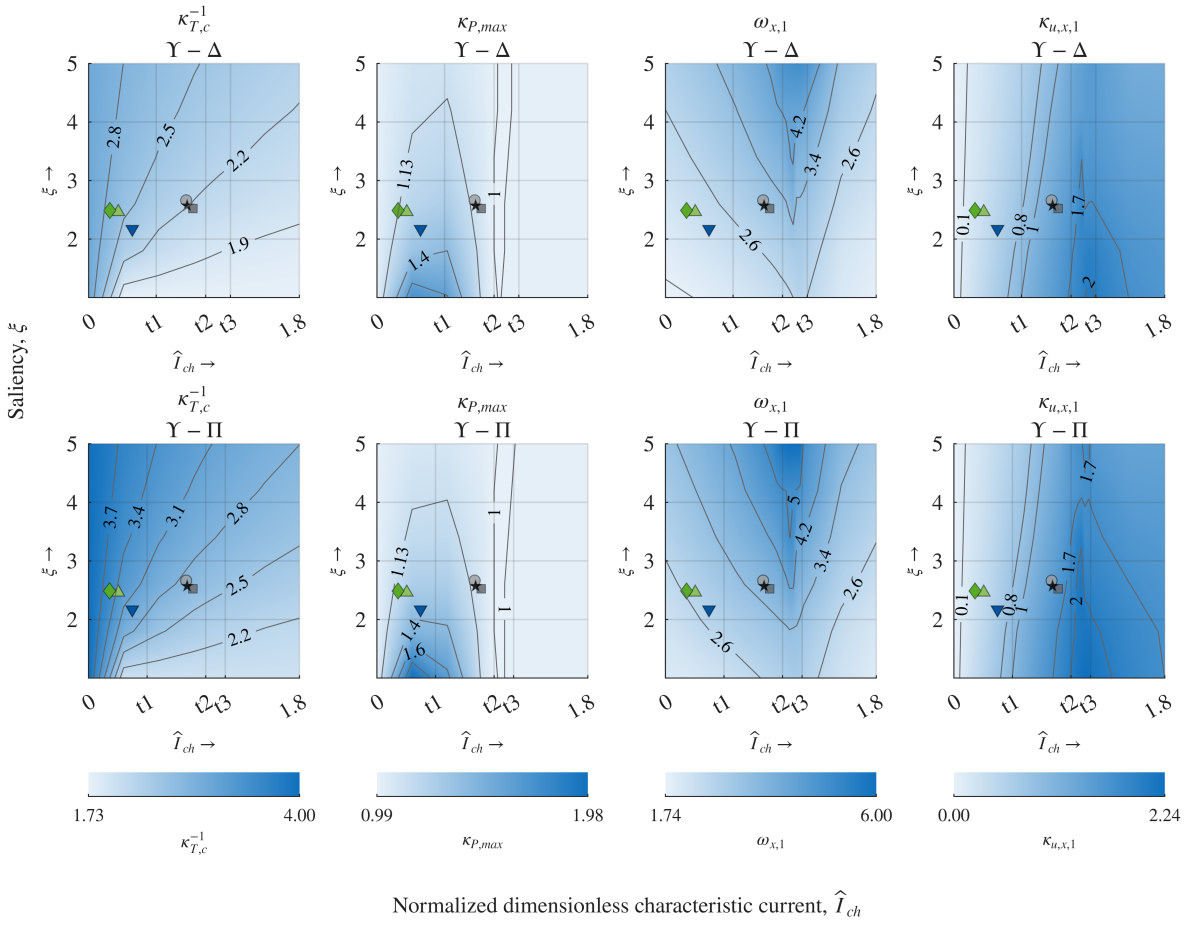


Figure 6. Single point metric: Maximum performance FoMs ($\kappa_{T,c}$, $\kappa_{P,\mathrm{max}}$) and Crossover point FoMs ($\hat{\omega}_{x,1}$, $\kappa_{u,x,1}$) for Y–Δ and Y–Π AWR topologies.

3.2. Crossover Point FoMs

The crossover FoMs identify where the reconfigured envelope begins to dominate the anchor envelope and the voltage stress associated with such a mode transition. Values of $\kappa_{u,x,1}$ above unity indicate that the open-circuit induced voltage exceeds the available DC-link voltage. Under a short-circuit condition, this can lead to a risk of uncontrolled generating operation if no active control is applied. In an open-circuit condition, the resulting terminal voltage must remain below the blocking-voltage rating of the inverter switching devices, as observed in [30].

Increasing ξ improves the anchor-state FW capability and therefore shifts the crossover to higher speed, while the dependence on $\hat{I_{\mathrm{ch}}}$ produces a ridge near $\hat{I_{\mathrm{ch}}} \approx 1$. Below this region, the reconfigured state extends useful high-speed operation; above it, the FW benefit weakens and the crossover speed decreases. The voltage-stress factor follows the same

ridge qualitatively, but is moderated by the reduction in $\hat{\Psi}_{\mathrm{PM}}$ with increasing ξ in the normalized model.

3.3. CPSR FoMs

The impact of the characteristic current $\hat{I_{\mathrm{ch}}}$ on the FW capability, and hence on CPSR and the torque–speed envelope FoM, as seen in Figure 7, is established with three thresholds defined by $\hat{I_{\mathrm{ch}}}$ and $k_{\mathrm{w,rec}}$:

- For $\hat{I_{\mathrm{ch}}} \leq \frac{1}{k_{\mathrm{w,rec}}}$, both $\kappa_{\mathrm{CPSR,env}}$ and $\kappa_{T,\mathrm{env}}$ increase with $\hat{I_{\mathrm{ch}}}$. However, the gain decreases with increasing ξ, since ξ improves the anchor state's own CPSR. Machines with moderate ξ show improvements of up to four times in CPSR from the analytical model. Machines with low ξ and low $\hat{I_{\mathrm{ch}}}$ show the largest improvement in $\kappa_{T,\mathrm{env}}$ of more than 20% over the anchor state.
- For $\frac{1}{k_{\mathrm{w,rec}}} < \hat{I_{\mathrm{ch}}} \leq \frac{k_{\mathrm{w,rec}}^3 - 1}{k_{\mathrm{w,rec}}(k_{\mathrm{w,rec}}^2 - 1)}$, the reconfigured state's finite maximum speed limits its advantage, and both ratios remain close to unity.
- For $\hat{I_{\mathrm{ch}}} > \frac{k_{\mathrm{w,rec}}^3 - 1}{k_{\mathrm{w,rec}}(k_{\mathrm{w,rec}}^2 - 1)}$, both states are speed-limited with a narrow CPSR; the ratios rise slightly above unity, but the absolute improvement stays limited to until just before $\hat{I_{\mathrm{ch}}} < 1 + \frac{1}{k_{w,rec}}$ which corresponds to the CPSR speed potential of both the anchor and reconfigured states being equal.

The composite envelope FoMs show that the largest AWR benefit occurs when reconfiguration moves the machine from a voltage-limited anchor state into a more favorable high-speed operating regime. This confirms that AWR should be evaluated by the composite envelope rather than by peak values alone.

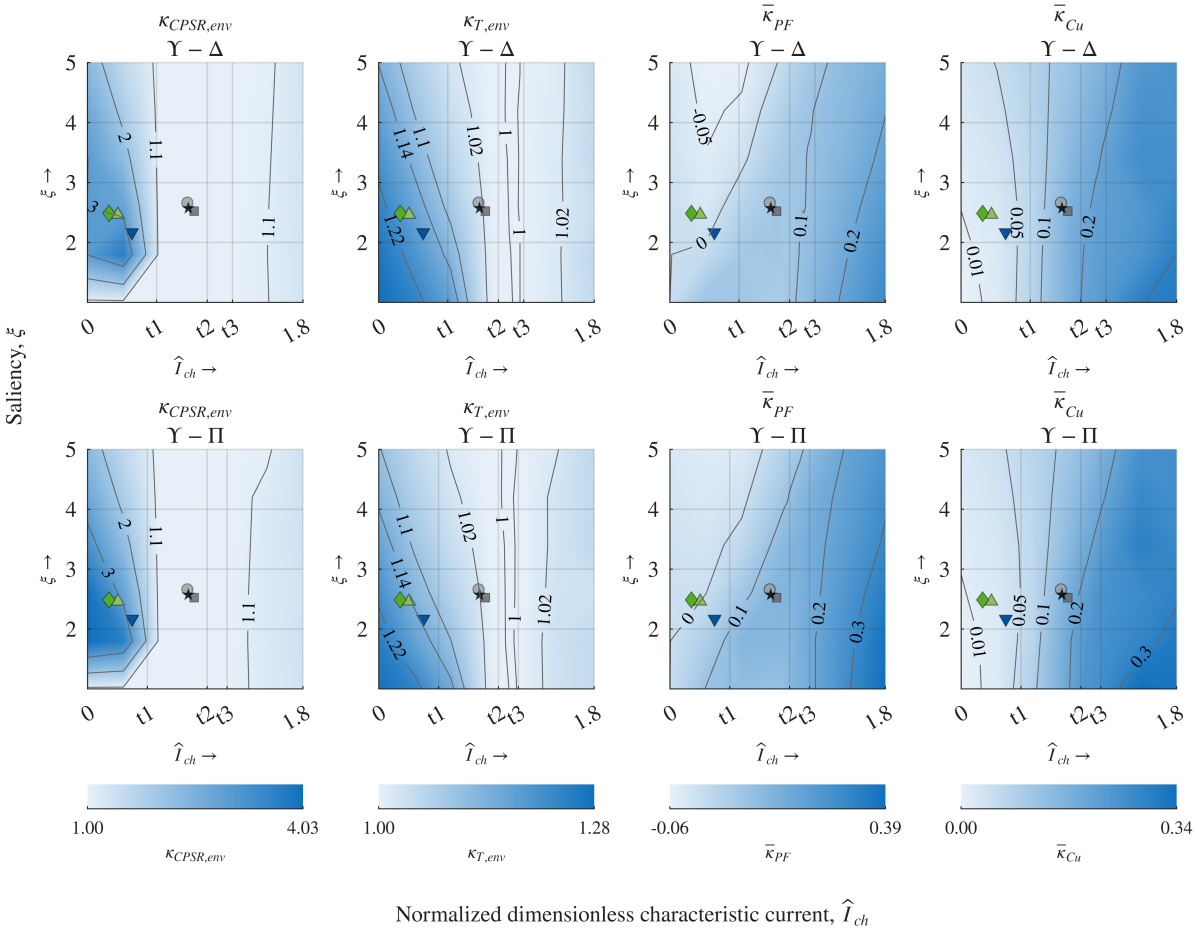


Figure 7. Envelope & area metrics: CPSR FoMs ($\kappa_{\mathrm{CPSR,env}}$, $\kappa_{T,\mathrm{env}}$) and part-load performance FoMs ($\bar{\kappa}_{PF}$, $\bar{\kappa}_{Cu}$) for Y–Δ and Y–Π AWR topologies.

3.4. Part-Load Performance FoMs

The FoMs described so far characterize performance along the rated torque–speed envelope only. To address part-load performance, two additional FoMs, $\bar{\kappa}_{PF}$ and $\bar{\kappa}_{Cu}$, are defined based on indicative power factor (PF) and ohmic losses, respectively. Though stator ohmic losses were neglected in the derivation of the normalized voltage and torque equations, a representation of these losses is useful for design analysis and is post-processed from the analytical model results [36].

Both FoMs are area-weighted means of the point wise difference between the reconfigured and anchor states, normalized over the common feasible operating region Ω_{common}; positive values indicate that reconfiguration is favorable. $\bar{\kappa}_{PF}$ captures the reduction in apparent power demand on the inverter for a given torque and speed, while $\bar{\kappa}_{Cu}$ captures the improvement in part-load efficiency through reduced stator ohmic (DC) loss.

Figure 7 shows $\bar{\kappa}_{PF}$ in the base-speed region improves with $\hat{I_{\text{ch}}}$ but degrades with ξ, whereas in deep FW the trend reverses. Since Ω_{common} is dominated by the base-speed region, and predominantly by that of the reconfigured state, $\bar{\kappa}_{PF}$ follows the base-speed trend: it decreases with ξ and increases with $\hat{I_{\text{ch}}}$.

Reconfiguration reduces phase current in the Δ state and the resistance R_{eff} in the Π state. As copper loss scales with I^2R_{eff}, the advantage is largest near the current limit and shrinks at part load. $\bar{\kappa}_{Cu}$ is further constrained by the definition of Ω_{common} itself: for $\hat{I_{\text{ch}}} \leq 1/k_{\text{w,rec}}$, a large fraction of the reconfigured envelope lies outside Ω_{common}. Therefore, the advantage is only partially captured, whereas at higher $\hat{I_{\text{ch}}}$ the overlap grows and the copper-loss reduction is more fully reflected in $\bar{\kappa}_{Cu}$.

3.5. Verification on Baseline Machines

The baseline machines M1–M6 (Table 5) are used to compare nonlinear FEA results against the extended NPP model at matched normalized design points. Measurement results of machine M3 are additionally included. The original winding connection is treated as the Y anchor, and the Δ state is obtained by reconfiguring the FEA models and the test machine M3 while holding geometry, materials, temperatures, system voltage and current limits as fixed boundary conditions. Switching transients and voltage stresses during reconfiguration were not experimentally investigated in this study.

The torque-speed curves from the FEA results and measurement results are normalized in the same normalization framework as the analytical model as from [36], restated in Appendix A. Corner speed of the anchor configuration is taken as the speed normalization reference ($\omega_{\text{m},0}$). Torque is normalized to the corner point speed with unity PF electrical power (T_0). The FEA-derived normalized characteristic current ($\hat{I_{\text{ch}}}$) and corner-point ξ locate each machine on the NPP to generate the corresponding analytical envelopes and FoMs.

For the machines M1-M6, Figure 8 shows the torque-speed envelopes. Figure 9 compares the analytical and FEA-based FoMs by showing both trend correlation and deviation as error. The dashed gray line in Figure 9 represents perfect agreement between the two models, corresponding to zero error. The dotted stems connecting the scatter points to this line visualize the individual errors. For The error distributions shown in Figure 10, each box spans the middle 50% of the error data (25th to 75th percentile), with the median denoted by the internal line, and whiskers extending to the most extreme non-outlier values. Data from the FoMs for machine M3 are provided in Table 7 and for all the machines including error metrics in Appendix E.

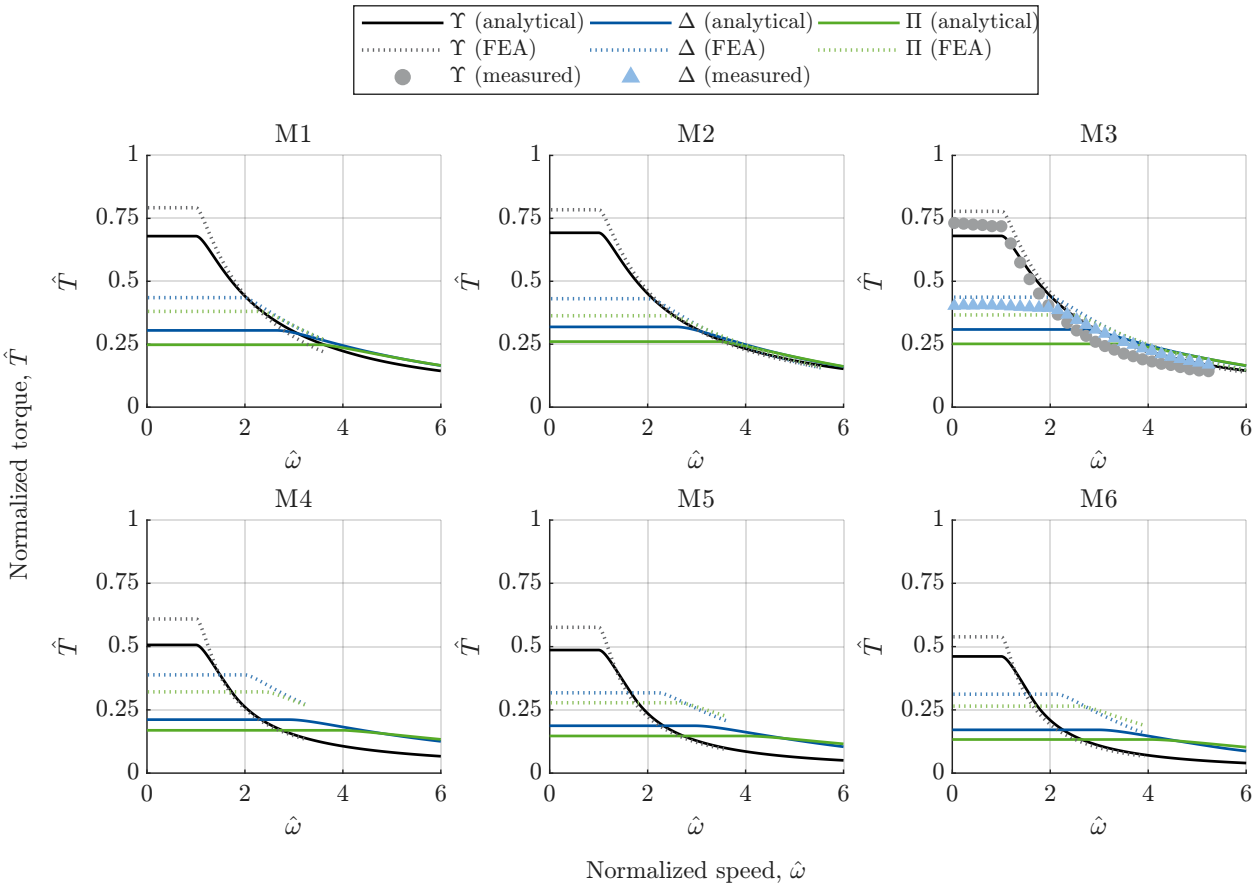


Figure 8. Torque–speed envelopes from FEA and the analytical NPP model for the Y–Δ pair across M1–M6.

The envelopes in Figure 8 show the largest discrepancies in the base-speed region, with good agreement in FW, consistent with prior literature [36]. The analytical model under-predicts peak torque for the reconfigured state, particularly at low $\hat{I_{\text{ch}}}$ and high ξ (Figure 11), i.e., machines with relatively higher current loading to magnetic loading. This is due to the constant-inductance NPP model not being able to capture current-dependent saturation resolved by FEA, an effect also reported in other works utilizing the analytical NPP model [36,40]. The measurement results from machine M3 show good agreement with the FEA results in FW region for both configurations. For both configuration, the maximum torque is in between the analytical and FEA results, while for the reconfigured configuration, the maximum torque is closer to the FEA results.

As a result of the non-linear saturation, the analytical model consistently overestimates $\kappa_{T,c}^{-1}$ particularly, at low $\hat{I_{\text{ch}}}$ (machines M3–M6). The error with the peak torque due to saturation effect in the reconfigured state, as represented in Figure 11, therefore also systematically impacts the analytical crossover point, $\omega_{x,1}$. The corner-point torque ratio, $\kappa_{T,c}$, has the largest error and practically no correlation. Therefore, it is not reliable as an absolute metric under the linear model, constant-inductance assumption. However, for $\omega_{x,1}$, the analytical model captures the relative trend, so this crossover point FoM is still useful for comparative screening purposes but not for absolute prediction.

Overall, the analytical model shows strong trend correlation for the FoMs covering composite CPSR, envelope expansion, peak-power ratio, crossover voltage-stress factor, and relative copper-loss improvement. The errors quantify the corresponding deviations and support the interpretation that these FoMs are suitable for relative preliminary design-space screening.

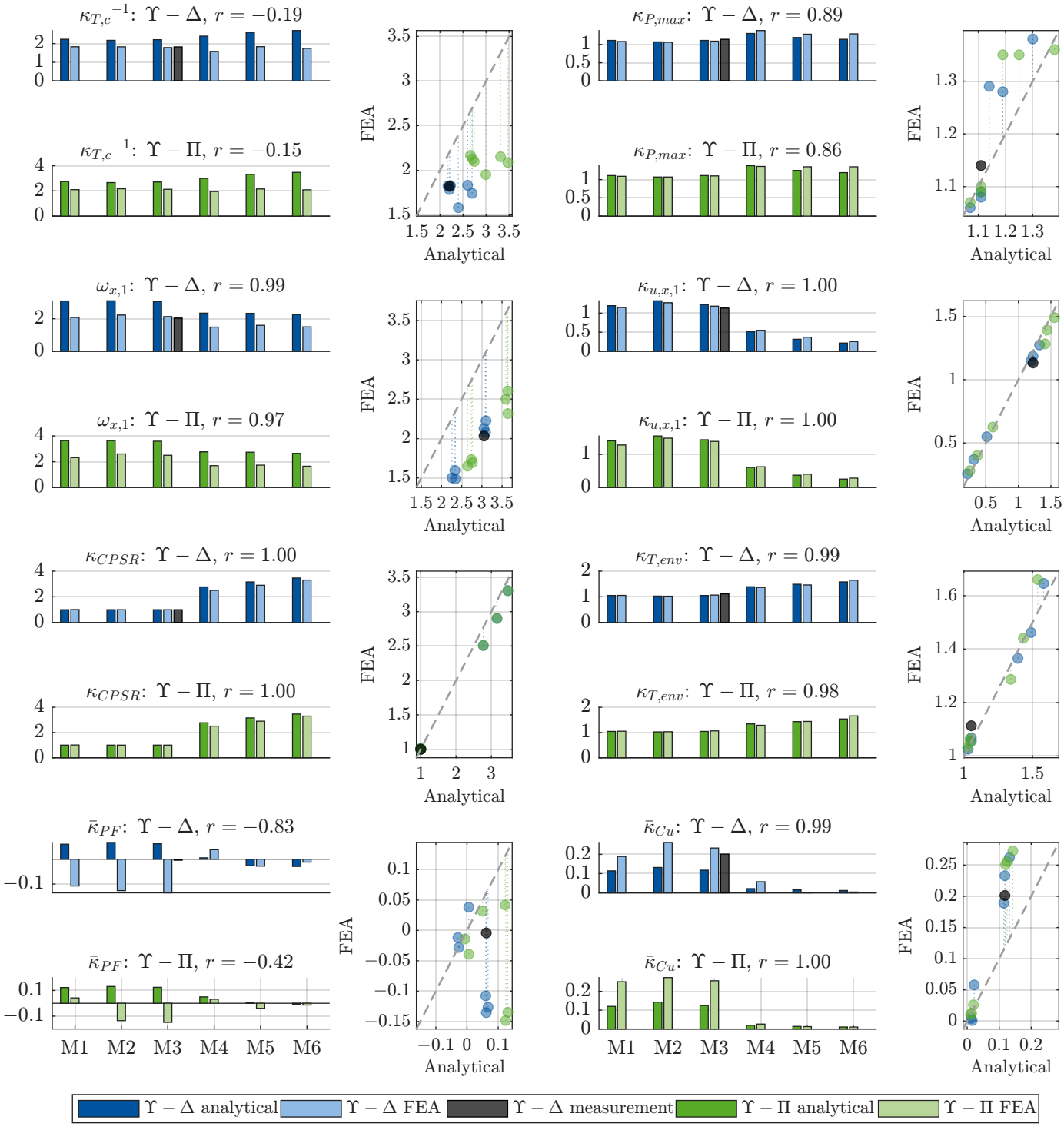


Figure 9. Comparison of analytical and FEA-based FoM values across M1–M6, including measurement results from machine M3; correlation coefficient r indicates trend agreement.

As seen in Figure 11, the current, torque and hence, also the PF non-linearities are not captured well by the analytical model especially in the base-speed as discussed also in [36], in their comparison between saturated and linear NPP model. Since Ω_{common} is dominated the base-speed region of the both states especially that of reconfigured state, $\bar{\kappa}_{PF}$ is prone to errors. As a result $\bar{\kappa}_{PF}$ is not reliable for design ranking because its trend is opposite to the FEA result. On the other hand, ohmic losses related FoM, $\bar{\kappa}_{Cu}$, shows deviation to analytical model, but the trends are catpured. Hence, this FoM can be used for relative screening in the design space but not for absolute prediction.

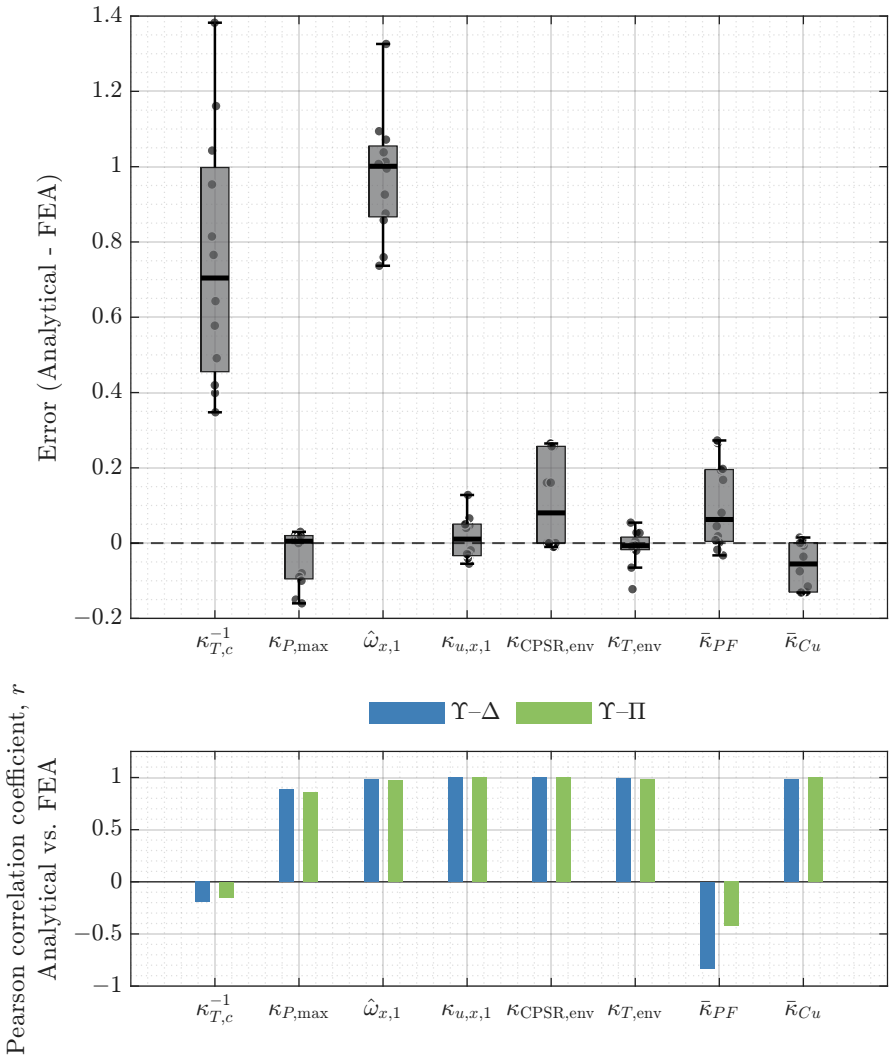


Figure 10. Distribution of deviation (shown as errors) and correlation coefficient between analytical and FEA-based FoM values across M1–M6, including measurement results from machine M3.

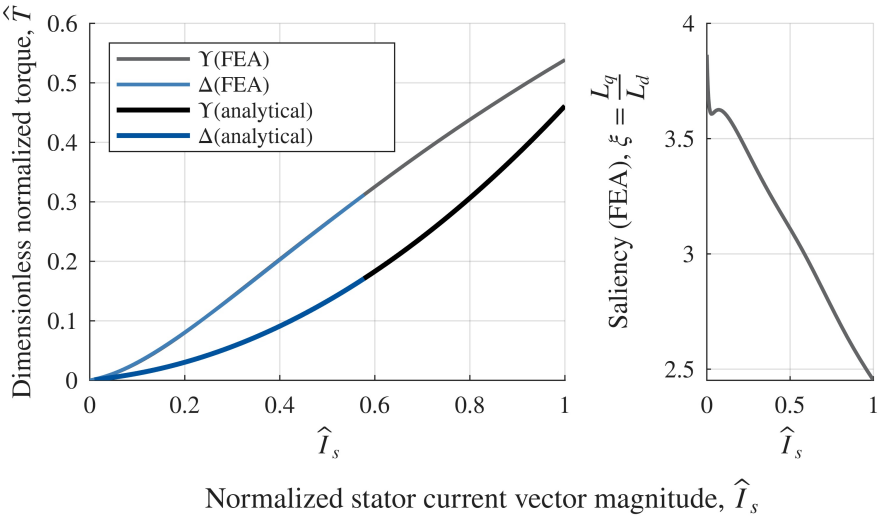


Figure 11. FEA vs. analytical NPP normalized torque–current characteristics for the Y–Δ pair, machine M6, base-speed region.

Table 7. Comparison of FoMs from analytical, FEA, and measurement results for machine M3.

Method	$\hat{I_{\mathrm{ch}}}$	ξ	$\kappa_{T,c}^{-1}$	$\kappa_{P,\max}$	$\hat{\omega}_{x,1}$	$\kappa_{u,x,1}$	$\kappa_{\mathrm{CPSR,env}}$	$\kappa_{T,\mathrm{env}}$	$\bar{\kappa}_{PF}$	$\bar{\kappa}_{Cu}$
Analytical			2.20	1.11	3.05	1.23	1.00	1.05	0.06	0.12
FEA [a]	0.84	2.57	1.78	1.09	2.13	1.18	1.00	1.07	−0.14	0.23
Measurement	0.81	2.66	1.82	1.14	2.03	1.13	1.00	1.11	−0.01	0.20

[a] FEA simulation for machine M3 was performed at same conditions as measurement, listed in Appendix C.

4. Discussion

The relevant transition regions in the normalized design space occur at three characteristic thresholds:

1. $t_1 : \hat{I_{\mathrm{ch}}} \leq \frac{1}{k_{\mathrm{w,rec}}}$ marks the region of maximum CPSR and torque–speed envelope improvement.
2. $t_2 : \hat{I_{\mathrm{ch}}} \approx 1$ is where maximum-power improvement flattens and crossover voltage stress become critical.
3. $t_3 : 1 < \hat{I_{\mathrm{ch}}} \leq \frac{k_{\mathrm{w,rec}}^3 - 1}{k_{\mathrm{w,rec}}(k_{\mathrm{w,rec}}^2 - 1)}$ is where torque–speed envelope improvement is least.

Thresholds t_1, t_2, and t_3 are analytical thresholds based on CPSR speed ratio of the lossless, linear NPP-based formulation used in this work. Their locations are given by $\hat{I}_{\mathrm{ch}}$ and $k_{\mathrm{w,rec}}$, whereas their locations can be offset when considering losses and saturation (25). The FoMs themselves depend on the selected speed range, normalization base, and common operating region, even if the thresholds are analytically fixed. For a meaningful comparison, the evaluated speed range should cover a wide enough normalized FW region and be referenced consistently to the corner point definition used in this framework.

In the present results, the FoMs associated with the composite CPSR, maximum-power ratio, torque-envelope improvement, crossover speed, and voltage-stress behaviour show characteristic contours around the threshold values. Saturation modifies the torque-current relationships, particularly around the base-speed peak torque and crossover regions, and can therefore influence the transition behaviour observed via FEA models of saturated machine designs. Accordingly, the thresholds should be interpreted as analytical design-region boundaries for normalized preliminary screening, rather than as universal physical transition points.

The key implications are summarized in Table 8. The analytical $\hat{I}_{\mathrm{ch}} - \xi$ NPP model shows poor to no agreement with torque and PF related FoMs, as also observed in the grounding framework in [36]. Agreement is better for envelope, CPSR and ohmic loss related FoMs which are valuable for determining benefits of AWR. Thus, based on these FoMs several design recommendations can be made for automotive traction machines with the AWR topologies considered.

Low ($\hat{I_{\mathrm{ch}}}$) designs

Machines with low Low ($\hat{I_{\mathrm{ch}}}$) benefit most from reconfiguration in terms of CPSR and torque–speed envelope expansion. The maximum benefit occurs up to a threshold value of $\hat{I_{\mathrm{ch}}} < \frac{1}{k_{\mathrm{w,rec}}}$. This observation motivates a design approach of reducing magnetic loading relative to current-loading, which in turn, can move the machine into the low-$\hat{I_{\mathrm{ch}}}$ region where reconfiguration yields stronger high-speed benefits. Following designs benefit most:

SynRM	designs without PM
PMaSynRM	designs with weaker magnets and higher current loading, and
IPMSM	designs with significantly reduced rare-earth magnet content.
SPMSM	designs with weaker magnets and higher current loading.

In all four cases, conventional designs required a trade-off with high speed performance and low-end torque. Reconfiguration significantly enhances the machine's high-speed performance and extends its operational range while saving on magnet material costs. The torque ratio from FEA models suggest availability of around $k_{\mathrm{w,rec}}$ times the torque in the anchor state as compared to the reconfigured state. This means the benefit in high-speed FoMs is achieved without compromising the low-speed torque requirements for traction applications.

Table 8. Key implications of the AWR comparison FoMs over the $(\hat{I_{\mathrm{ch}}}, \xi)$ parameter plane, including correlation trend with FEA models.

FoM	Symbol	Key Implication (Design Message)	FEA Agreement
		Maximum performance FoMs	
Corner-point torque ratio	$\kappa_{T,c}$	Reconfiguration incurs a base-speed torque penalty relative to the anchor state; the disadvantage is most pronounced at low $\hat{I_{\mathrm{ch}}}$ and high ξ.	Low
Peak power ratio	$\kappa_{P,\max}$	Peak-power benefit depends on $\hat{I_{\mathrm{ch}}}$: for $\hat{I_{\mathrm{ch}}} \geq 1$, reconfiguration does not increase the achievable peak power, independent of ξ.	High
		Crossover point FoMs	
First crossover speed	$\hat{\omega}_{x,1}$	Reconfiguration becomes advantageous at lower speed when both $\hat{I_{\mathrm{ch}}}$ and ξ are low; Δ tends to earlier crossover than Π due to its lower $k_{\mathrm{w,rec}}$.	Trends only
Crossover voltage-stress factor	$\kappa_{u,x,1}$	The highest voltage stress and associated mode-shift risk occur near $\hat{I_{\mathrm{ch}}} \approx 1$ across ξ; Δ generally yields lower stress than Π.	High
		CPSR FoMs	
Composite AWR CPSR	$\kappa_{\mathrm{CPSR,env}}$	$\hat{I_{\mathrm{ch}}}$ determines CPSR gain: strong improvement occurs for $\hat{I_{\mathrm{ch}}} \leq 1/k_{\mathrm{w,rec}}$, while designs near $\hat{I_{\mathrm{ch}}} \approx 1$ show negligible benefit; higher ξ reduces the relative gain.	High
Composite torque-envelope area ratio	$\kappa_{T,\mathrm{env}}$	Torque–speed area expands significantly for $\hat{I_{\mathrm{ch}}} \leq 1/k_{\mathrm{w,rec}}$, with the largest gains at low ξ; for $1 < \hat{I_{\mathrm{ch}}} < \frac{k_{\mathrm{w,rec}}^3 - 1}{k_{\mathrm{w,rec}}(k_{\mathrm{w,rec}}^2 - 1)}$, no gain is expected.	High
		Part-load performance FoMs	
Mean PF improvement	$\bar{\kappa}_{PF}$	Improvement is favored by higher $\hat{I_{\mathrm{ch}}}$ and lower ξ; low $\hat{I_{\mathrm{ch}}}$ combined with high ξ can lead to deterioration.	Low
Mean copper-loss improvement	$\bar{\kappa}_{Cu}$	Reconfiguration can reduce part-load ohmic losses even when envelope gains are small, subject to the common operating area; for the same parameters, Y–Π gives a larger reduction than Y–Δ.	Trends only

Designs with $\hat{I_{\mathrm{ch}}} \approx 1$

Designs with $\hat{I_{\mathrm{ch}}} \approx 1$ which make up most conventional rare-earth magnet based traction IPMSM designs, show limited gains in CPSR and torque–speed envelope from reconfiguration. However, they benefit in part-load ohmic losses, particularly during high-speed FW operation. Thus, the motivation here is that for designs with strong-magnet machines which suffer higher losses in FW, reconfiguration can mitigate part of these losses by optimizing the operating point. An alternative design approach is to reduce magnetic strength and material cost to utilize the potential of reconfiguration as mentioned in the previous point. However, it is to be noted that while the analytical model shows benefit in part-load PF FoM, FEA models show deterioration. Overall losses and efficiency, therefore, need detailed evaluation beyond the preliminary screening offered by the analytical NPP model.

Designs with high $\hat{I_{ch}}$

For machines with high $\hat{I_{ch}}$, i.e., with high magnetic strength and low current loading with limited FW capability, reconfiguration may not improve the rated maximum power. It does, however, improve the torque–speed envelope and part-load ohmic losses, thereby providing a viable route to extend speed range despite limited FW capability.

Choice between reconfiguration pairs

The absolute improvement in high speed performance and torque–speed envelope FoMs is higher for Y–Π reconfiguration pair than the Y–Δ pair. This follows from the larger effective reconfiguration factor $k_{w,rec}$ of the Y–Π pair. However, following aspects favor Y–Δ pair:

1. The crossover speed is lower for the Y–Δ pair, hence, the benefits are already available at lower speeds.
2. The crossover voltage-stress is lower for the Y–Δ pair, hence, the risk of mode-shift is lower.
3. The threshold value for CPSR and torque–speed envelope improvement is inversely proportional to $k_{w,rec}$. More machine designs are covered by the Y–Δ pair than the Y–Π pair.

Limitations

The present study is intentionally limited to high-level, geometry-independent, normalized, scalable AWR screening for machine designs. The objective of this work is the relative identification of AWR-favorable regions in the normalized design space before deeper electromagnetic FEA based design space exploration.

Temperature-dependent electromagnetic and resistive properties, are neglected assuming equal thermal conditions for the envelopes. In practice transient thermal conditions influence the continuous operation capabilities and are not addressed in this study. Copper utilization and its impact on losses are also neglected in this analytical lossless framework.

Triplen-harmonic circulating currents in the Δ connection are not represented by the fundamental-wave *d*-*q* model, which is consistent with the present scope. In such machines, circulating currents can represent a significant fraction of the maximum fundamental current rating, also impacting losses. These require dedicated voltage-source transient simulations and measurement equipment. These are are outside the scope of the present work.

Torque ripple is outside the present steady-state fundamental envelope analysis. However, torque ripple may differ between configurations through the saturation dependent harmonic effects such as with delta-winding connection and requires dedicated voltage-source, time-domain and harmonic investigation

Reconfiguration transients and inverter switching dynamics of active and online winding reconfiguration are not considered because the model addresses steady-state operating envelopes. Switching transients and voltage stresses during reconfiguration were not experimentally investigated, but they remain important for implementation and control validation and are left for future work.

5. Conclusions

This work addressed the need for a geometry-independent method to assess when AWR is beneficial for traction PMSM designs. Overall, the three goals stated in the introduction were achieved. First, the $\hat{I_{ch}}$-based NPP model was extended to AWR by introducing topology-dependent reconfiguration factors, $k_{w,rec}$, for the Y–Δ and Y–Π configurations, while keeping the Y machine as the normalization anchor.The resulting model predicts

the torque-speed-power behavior of AWR topologies over the $\hat{I_{ch}}$–ξ design space. Second, a reduced set of FoMs are presented to quantify reconfiguration benefit across peak performance, crossover behavior, CPSR, torque-speed envelope expansion, and part-load performance. Third, from $\hat{I_{ch}}$ and $k_{w,rec}$, a definition of CPSR potential speed ratio between the reconfigured and anchor state gives analytically three thresholds at $\hat{I_{ch}} = \frac{1}{k_{w,rec}}$, $\hat{I_{ch}} = 1$, and $\hat{I_{ch}} = \frac{k_{w,rec}^3 - 1}{k_{w,rec}(k_{w,rec}^2 - 1)}$. These thresholds separate favorable and unfavorable regions for AWR benefits within the scope of FoMs of composite CPSR, envelope expansion, peak-power ratio, crossover voltage-stress factor.

Together they show that the benefits from AWR for a given machine type depend on its position in the $\hat{I_{ch}}$–ξ parameter plane for a given $k_{w,rec}$. The primary result is that the normalized characteristic current is the dominant design parameter because it captures the relative strength of PM flux linkage, or magnetic loading, with respect to current loading.

Comparison with nonlinear FEA results for six representative traction-machine designs. Measurement results from one machine (M3) covering steady-state characteristics without active reconfiguration switching is also compared. These confirmed that the analytical model captures the main system-level trends, including composite CPSR, envelope expansion, peak-power ratio, crossover voltage-stress factor, and relative copper-loss improvement. Torque ratio and part-load power-factor metrics are the least reliable of the presented metrics compared with the FEA model, due to the absence of nonlinear saturation effects in the analytical model. The extended analytical NPP model is therefore suitable for early-stage design screening and for identifying machine concepts that can benefit from reconfiguration, while final performance prediction still requires nonlinear FEA due to saturation-dependent inductance effects influencing several important peak-performance and part-load loss metrics.

Overall, the proposed NPP-based framework provides a compact design-screening tool for exploring AWR machine concepts and identifying promising regions of the design space before detailed electromagnetic optimization.

Author Contributions: Conceptualization, R.K.-K., H.W. and J.A.; methodology, R.K.-K.; formal analysis, R.K.-K.; investigation, R.K.-K., H.W. and H.C.; writing—original draft preparation, R.K.-K.; writing—review and editing, H.W., H.C., M.E. and J.A.; visualization, R.K.-K.; supervision, M.E. and J.A.; resources, M.E. and J.A.; funding acquisition, M.E. and J.A. All authors have read and agreed to the published version of the manuscript.

Funding: This work was supported by the European Union's Horizon Europe research and innovation program under Grant Agreement No.101192720 (HIGH-VOLTAGE FAST-CHARGING EFFICIENT ELECTRIC VEHICLE POWERTRAINS).

Data Availability Statement: The original measured and simulated torque-speed envelope data presented in this study are openly available in the Zenodo repository at https://doi.org/10.5281/zenodo.22647758.

Acknowledgments: The authors acknowledge Onur Kara, Fabian Jonczyck, and Oliver Kusche from the Chair of Mechatronics in Mobile Propulsion, RWTH Aachen University for support with measurements. The authors also acknowledge Michael Schröder and Christoph Neuhaus from FEV Europe GmbH, as well as Christian Milwisch and Peter Pišek, from Magna Powertrain GmbH, for their support.

Conflicts of Interest: The authors declare no conflicts of interest.

Abbreviations

SynRM	Synchronous reluctance machine
PM	Permanent magnet
PMaSynRM	Permanent magnet assisted synchronous reluctance machine
PMSM	Permanent magnet synchronous machine
IPMSM	Interior permanent magnet synchronous machine
SPMSM	Surface-mounted permanent magnet synchronous machine
EESM	Electrically excited synchronous machine
AWR	Active winding reconfiguration
NPP	Normalized Parameter Plane
CPSR	Constant power speed range
FoM	Figure of Merit
MTPA	Maximum torque per ampere
MTPV	Maximum torque per voltage
FW	Field weakening
PF	Power factor
FEA	Finite element analysis
NdFeB	Neodymium iron boron
DC	Direct current
LUT	Look-up table
2D	Two-dimensional
IGBT	Insulated gate bi-polar transistor
e.g.	exempli gratia
i.e.	id est

Appendix A. Base Quantities for the NPP Model

Table A1. Base quantities for the NPP model.

Quantity	Base Definition	Normalized Quantities
Current	$I_0 = I_{\mathrm{lim}}$	$\hat{I_{\mathrm{lim}}}$, $\hat{I_{\mathrm{d}}}$, $\hat{I_{\mathrm{q}}}$, $\hat{I_{\mathrm{ch}}}$
Voltage	$U_0 = U_{\mathrm{lim}}$	$\hat{U_{\mathrm{lim}}}$, $\hat{U_{\mathrm{d}}}$, $\hat{U_{\mathrm{q}}}$
Power	$P_{\mathrm{el},0} = \frac{3}{2} U_{\mathrm{lim}} I_{\mathrm{lim}}$	$\hat{P}$
Flux linkage	$\Psi_0 = U_{\mathrm{lim}}/\omega_{\mathrm{e},0}$; $\Psi_0 = \sqrt{\Psi_{\mathrm{d}}^2 + \Psi_{\mathrm{q}}^2}$	$\hat{\Psi_{\mathrm{PM}}}$, $\hat{\Psi_{\mathrm{d}}}$, $\hat{\Psi_{\mathrm{q}}}$
Electrical speed	$\omega_{\mathrm{e},0}$: speed at which the voltage-limit ellipse meets the current-limit circle at the MTPA point	$\hat{\omega_{\mathrm{e}}}$
Mechanical speed	$\omega_{\mathrm{m},0} = \omega_{\mathrm{e},0}/p$	ω_{m}
Inductance	$L_0 = \Psi_0/I_{\mathrm{lim}}$	$\hat{L_{\mathrm{d}}}$, $\hat{L_{\mathrm{q}}}$
Torque	$T_0 = P_{\mathrm{el},0}/\omega_{\mathrm{m},0} = \frac{3}{2} p \Psi_0 I_{\mathrm{lim}}$	$\hat{T_{\mathrm{e}}}$

Appendix B. Derivation of Ideal CPSR Capability Ratio and Threshold Values

Assuming maximum available d-axis current, and zero q-Axis current within the current limit circle,

$$\hat{I_d} = -\hat{I_{\mathrm{lim}}} \qquad \hat{I_q} = 0 \tag{A1}$$

Using the lossless steady-state voltage relation from Equations (1)–(4),

$$\hat{U_{\mathrm{lim}}}^2 = \hat{\omega_0}^2 \left[\left(\hat{L_d} \hat{I_d} + \hat{\Psi_{PM}} \right)^2 + \left(\hat{L_q} \hat{I_q} \right)^2 \right], \tag{A2}$$

and applying Equation (10), we get a relationship for a speed

$$\hat{U_{\text{lim}}} = \hat{\omega_0}\hat{L_d}(\hat{I_{\text{ch}}} - \hat{I_{\text{lim}}}) \tag{A3}$$

$$\hat{\omega_0} = \frac{\hat{U_{\text{lim}}}}{\hat{L_d}(\hat{I_{\text{ch}}} - \hat{I_{\text{lim}}})} \tag{A4}$$

Similarly it can be shown that with ohmic voltage drop, the expression is:

$$\hat{\omega_0} = \frac{\hat{U_{\text{lim}}}}{\hat{L_d}(\hat{I_{\text{ch}}} - \hat{I_{\text{lim}}}) + \hat{R_s}(-\hat{I_{\text{lim}}})} \tag{A5}$$

$$\textit{where} \qquad \hat{R_s} = \frac{U_{ohmic,drop,lim}}{U_0} = \frac{R_s I_{lim}}{U_0} \tag{A6}$$

The relationship with $\hat{I_{\text{ch}}}$ and $\hat{I_{\text{lim}}}$ is however, also a reference to inferred CPSR capability as observed in [36] and similar works around characteristic current [33,35,41]:

- For $\hat{I_{\text{ch}}} < \hat{I_{\text{lim}}}$, the voltage limit ellipses collapse to a point at $\hat{I_{\text{ch}}}$ within the current-limit circle. Theoretically infinite speed is possible but power, $\hat{P_{w,max}} \rightarrow \hat{I_{\text{ch}}}$, thus limiting the CPSR to a finite value.
- For $\hat{I_{\text{ch}}} = \hat{I_{\text{lim}}}$, theoretical infinite CPSR is achieved.
- For $\hat{I_{\text{ch}}} > \hat{I_{\text{lim}}}$, Torque and power capability collapse at a finite speed at $\hat{I_{\text{d}}} = \hat{I_{\text{lim}}} < \hat{I_{\text{ch}}}$, as the voltage ellipses of higher speeds lie entirely outside the current limit circle. Thus, limiting CPSR to a finite value. In fact, for this case (A4) is the maximum no-load speed equation.

The magnitude $|\hat{I_{\text{ch}}} - \hat{I_{\text{lim}}}|$, thus represents the reduction in infinite CPSR potential. Consequently, the speed $|\hat{\omega_0}|$ in (A4) is a representation of the CPSR potential. The ratio of the CPSR potential speed between reconfigured state to anchor state is then of interest, when considering the overall torque-speed envelope from AWR topologies.

For the anchor state,

$$\hat{U_{\text{lim,anc}}} = 1 \qquad \hat{I_{\text{lim,anc}}} = 1 \tag{A7}$$

and therefore

$$\hat{\omega_{0,\text{anc}}} = \frac{1}{\hat{L_{d,\text{anc}}}(\hat{I_{\text{ch,anc}}} - 1)} \tag{A8}$$

For the Y–Δ state,

$$\hat{U_{\text{lim,rec}}} = k_{\text{w,rec}} \qquad \hat{I_{\text{lim,rec}}} = \frac{1}{k_{\text{w,rec}}} \qquad \hat{I_{\text{ch,rec}}} = \hat{I_{\text{ch,anc}}} \qquad \hat{L_{d,\text{rec}}} = \hat{L_{d,\text{anc}}} \tag{A9}$$

which gives

$$\hat{\omega_{0,\text{rec}}} = \frac{k_{\text{w,rec}}}{\hat{L_{d,\text{anc}}}(\hat{I_{\text{ch,anc}}} - \frac{1}{k_{\text{w,rec}}})} \tag{A10}$$

For the Y–Π state

$$\hat{U_{\text{lim,rec}}} = 1 \qquad \hat{I_{\text{lim,rec}}} = 1 \qquad \hat{I_{\text{ch,rec}}} = k_{\text{w,rec}}\hat{I_{\text{ch,anc}}} \qquad \hat{L_{d,\text{rec}}} = \frac{\hat{L_{d,\text{anc}}}}{k_{\text{w,rec}}^2} \tag{A11}$$

which gives

$$\hat{\omega_{0,\text{rec}}} = \frac{1}{\frac{\hat{L_{d,\text{anc}}}}{k_{\text{w,rec}}^2}(k_{\text{w,rec}}\hat{I_{\text{ch,anc}}} - 1)} = \frac{k_{\text{w,rec}}}{\hat{L_{d,\text{anc}}}(\hat{I_{\text{ch,anc}}} - \frac{1}{k_{\text{w,rec}}})} \tag{A12}$$

Hence, both reconfiguration cases yield the same ratio of magnitude of the CPSR potential speeds:

$$r_\omega = \left| \frac{\omega_{\hat{0},\text{rec}}}{\omega_{\hat{0},\text{anc}}} \right| \tag{A13}$$

$$= \left| \frac{k_{\text{w,rec}}(\hat{I_{\text{ch}}} - 1)}{\hat{I_{\text{ch}}} - \frac{1}{k_{\text{w,rec}}}} \right| \tag{A14}$$

The first threshold follows from the reconfigured-state having infinite CPSR, i.e., $r_\omega \to \infty$. Setting,

$$\hat{I_{\text{ch}}} - \frac{1}{k_{\text{w,rec}}} = 0 \tag{A15}$$

Thus,

$$t_1 : \qquad \hat{I_{\text{ch}}} = \frac{1}{k_{\text{w,rec}}} \tag{A16}$$

The second threshold follows from the anchor-state to have infinite CPSR, i.e., $r_\omega \to 0$. Setting

$$k_{\text{w,rec}}(\hat{I_{\text{ch}}} - 1) = 0 \qquad\qquad t_2 : \hat{I_{\text{ch}}} = 1 \tag{A17}$$

The third threshold is defined by

$$r_\omega = \frac{1}{k_{\text{w,rec}}} \tag{A18}$$

Solving (A14) and (A18) for $\hat{I_{\text{ch}}} = \hat{I_{\text{ch,anc}}}$

$$\left| \frac{k_{\text{w,rec}}(\hat{I_{\text{ch}}} - 1)}{\hat{I_{\text{ch}}} - \frac{1}{k_{\text{w,rec}}}} \right| = \frac{1}{k_{\text{w,rec}}} \tag{A19}$$

We get,

$$t_3 : \qquad \hat{I_{\text{ch}}} = \frac{k_{\text{w,rec}}^3 - 1}{k_{\text{w,rec}}(k_{\text{w,rec}}^2 - 1)} \tag{A20}$$

This can also be written as

$$t_3 = 1 + \frac{1}{k_{\text{w,rec}}(k_{\text{w,rec}} + 1)} \tag{A21}$$

When considering ohmic voltage drop, the thresholds can be shown to solve to :

$$t_1 : \qquad \hat{I_{\text{ch}}} = \frac{1}{k_{\text{w,rec}}} + \frac{\hat{R_s}}{\hat{L_d}} \tag{A22}$$

$$t_2 : \qquad \hat{I_{\text{ch}}} = 1 + \frac{\hat{R_s}}{\hat{L_d}} \tag{A23}$$

$$t_3 : \qquad \hat{I_{\text{ch}}} = \frac{k_{\text{w,rec}}^3 - 1}{k_{\text{w,rec}}(k_{\text{w,rec}}^2 - 1)} + \frac{\hat{R_s}}{\hat{L_d}} \tag{A24}$$

Other values of note include,

$$\lim_{\hat{I_{\text{ch}}} \to 0} r_\omega = k_{\text{w,rec}}^2 \tag{A25}$$

$$\lim_{\hat{I_{\text{ch}}} \to \infty} r_\omega = k_{\text{w,rec}} \tag{A26}$$

The CPSR potential speed ratio balance point is obtained from $r_\omega = 1$, which gives,

$$\hat{I_{\text{ch}}} = 1 + \frac{1}{k_{\text{w,rec}}} \tag{A27}$$

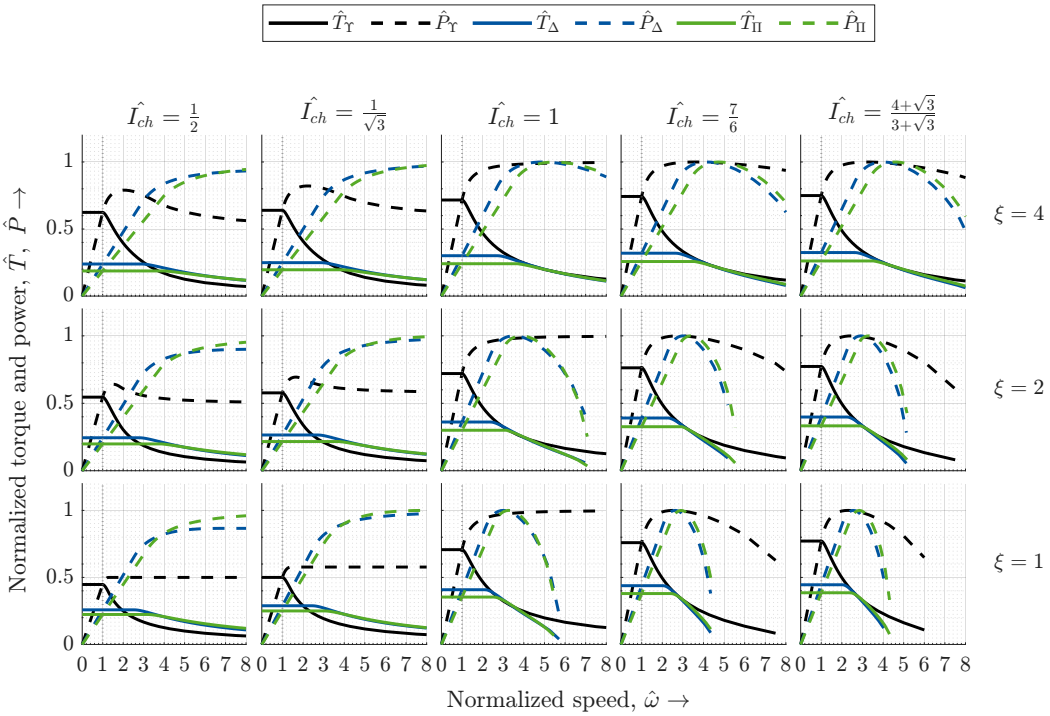


Figure A1. Torque-speed envelopes of the different reconfiguration pairs at the important threshold values of $\hat{I_{\text{ch}}}$.

Table A2. Thresholds and characteristic values from the CPSR potential speed ratio, r_ω.

Condition	$\hat{I_{ch}}$ Expression	$\hat{I_{ch,\Upsilon-\Delta}}$ Value	$\hat{I_{ch,\Upsilon-\Pi}}$ Value	r_ω Expression	$r_{\omega,\Upsilon-\Delta}$ Value	$r_{\omega,\Upsilon-\Pi}$ Value
Very low $\hat{I_{\text{ch}}}$	$\hat{I_{\text{ch}}} \to 0$	0	0	$\lim_{\hat{I_{\text{ch}}} \to 0} r_\omega = k_{\text{w,rec}}^2$	3	4
t_1	$\hat{I_{\text{ch}}} = \frac{1}{k_{\text{w,rec}}}$	$\frac{1}{\sqrt{3}}$	$\frac{1}{2}$	$r_\omega(t1)$	∞	∞
t_2	$\hat{I_{\text{ch}}} = 1$	1	1	$r_\omega(t2)$	0	0
t_3	$\hat{I_{\text{ch}}} = \frac{k_{\text{w,rec}}^3 - 1}{k_{\text{w,rec}}(k_{\text{w,rec}}^2 - 1)}$	$\frac{4+\sqrt{3}}{3+\sqrt{3}}$	$\frac{7}{6}$	$r_\omega(t3) = \frac{1}{k_{\text{w,rec}}}$	$\frac{1}{\sqrt{3}}$	$\frac{1}{2}$
r_ω unity	$\hat{I_{\text{ch}}} = 1 + \frac{1}{k_{\text{w,rec}}}$	$\frac{\sqrt{3}+1}{\sqrt{3}}$	$\frac{3}{2}$	$r_\omega = 1$	1	1
Very high $\hat{I_{\text{ch}}}$	$\hat{I_{\text{ch}}} \to \infty$	∞	∞	$\lim_{\hat{I_{\text{ch}}} \to \infty} r_\omega = k_{\text{w,rec}}$	$\sqrt{3}$	2

Appendix C. Machine M3 Dynamometer Test Bench Setup and Operating Conditions

Table A3. Numbered components and measurement equipment of the dynamometer test bench for machine M3 shown in Figure 5.

No.	Component	Function/Equipment	Equipment Manufacturer/Source [a]
1	Device under test	Machine M3, operated in Y and Δ winding configurations.	MOBIS Parts Europe, Sandersdorf-Brehna, Germany
2	Reconfiguration terminal box	Terminal box at the open-ended winding terminals of DUT for manual winding reconfiguration between Y and Δ.	Custom-built prototype, RWTH Aachen University, Germany
3	Inverter terminal box and electrical sensor unit	Three-phase cable hand-over from inverter to reconfiguration terminal, as well as housing for 3-phase current sensors (LEM-ITS 600) and Voltage probes	Custom Prototype; Current sensors and voltage probes: LEM International SA, Meyrin, Switzerland
4	Inverter	Universal inverter operating the device under test	Inverter: AixControl GmbH, Aachen, Germany; Controller: dSpace GmbH, Paderborn, Germany; Field-oriented-control: Chair of Mechatronics in Mobile Propulsion, RWTH Aachen University, Germany
5	Electrical signal acquisition	Matuschek PowerAnalyzer used for recording electrical signals.	Matuschek Meßtechnik GmbH, Alsdorf, Germany
6	Torque and speed measurement	HBM T40B torque transducer used for shaft torque and speed measurement.	Hottinger Brüel & Kjaer GmbH, Darmstadt, Germany
7	Load machine	High-speed dynamometer imposing the speed set-point.	Test-bench automation: FEV Europe GmbH, Aachen, Germany; Load machine: OSWALD Elektromotoren GmbH, Miltenberg, Germany
8	Cooling system	Closed-loop cooling water thermal conditioning unit. DUT has an oil-water heat exchanger.	Center for Mobile Propulsion, RWTH Aachen University, Germany

[a] Provided for information (lege artis) only. Apart from RWTH Aachen University, strictly no affiliation in any form to the study or to the authors.

Table A4. Operating conditions for machine M3 measurements.

Parameter	Value/Description
DC-link voltage	650 V
Control strategy	Field-oriented control with space-vector PWM
Modulation index	0.924
Stator winding temperature	318(5) K

Appendix D. FEA Modeling of the Baseline Machines

The modeling workflow is organized into three levels:

1. 2D FEA of a single operating-point: The two-dimensional cross-section of the machine including the active parts of stator and rotor laminations, the PM, and the air gap is modelled. Based on the number of poles and slots, geometry and winding configuration, only a section (for e.g., one pole section) of the whole machine is modelled based on assumptions of symmetry and continuity of electromagnetic fields. For this selected section, a mesh is generated and fields are calculated (Figure A2). The electromagnetic field solution is post-processed to determine output quantities such as flux linkages, currents, voltages, torque, torque ripple, and losses at each simulated operating point. Five loss mechanisms are addressed: core loss in the stator and

rotor laminations based on modified and improved generalized Steinmetz equation coefficient curve fitting [42,43], magnet eddy-current loss [44], ohmic losses (DC and AC winding [45]), and friction loss. PWM switching losses and stray load losses are neglected. Other standard assumptions for 2D FEA of rotating machinery apply :

- Stator windings are driven by ideal balanced sinusoidal three-phase current excitation. Supply harmonics, inverter switching effects, and control dynamics are neglected.
- The electromagnetic field is solved using transient 2D FEA with prescribed rotor motion.
- End effects and end-winding leakage inductances are not accounted for in the 2D FEA, rather they are accounted for separately.
- Laminated core is modeled with isotropic magnetic properties and a stacking factor of 0.97. Inter-lamination eddy currents are assumed to be negligible.
- Fixed uniform temperature, and mechanically rigid body at each simulated operating point.

2. Saturation and losses LUT: FEA is carried out across the full i_d–i_q plane at a fixed speed matching the corresponding measurements; the resulting LUT of output quantities are stored as scalable coefficients [46]. These are then used to evaluate results for any other speed, current, or torque set point.
3. Scaled models operating points sweep and losses evaluation: The method is extended to further scaling to different turns-ratio, axial length, voltage- and current-limits [27,47].

A 2D FEA model is used here because the normalized FoMs target the steady-state fundamental-wave torque–speed envelope and all machines are compared under identical assumptions. It provides acceptable accuracy relative to three-dimensional FEA, while balancing fidelity against simulation time and cost.

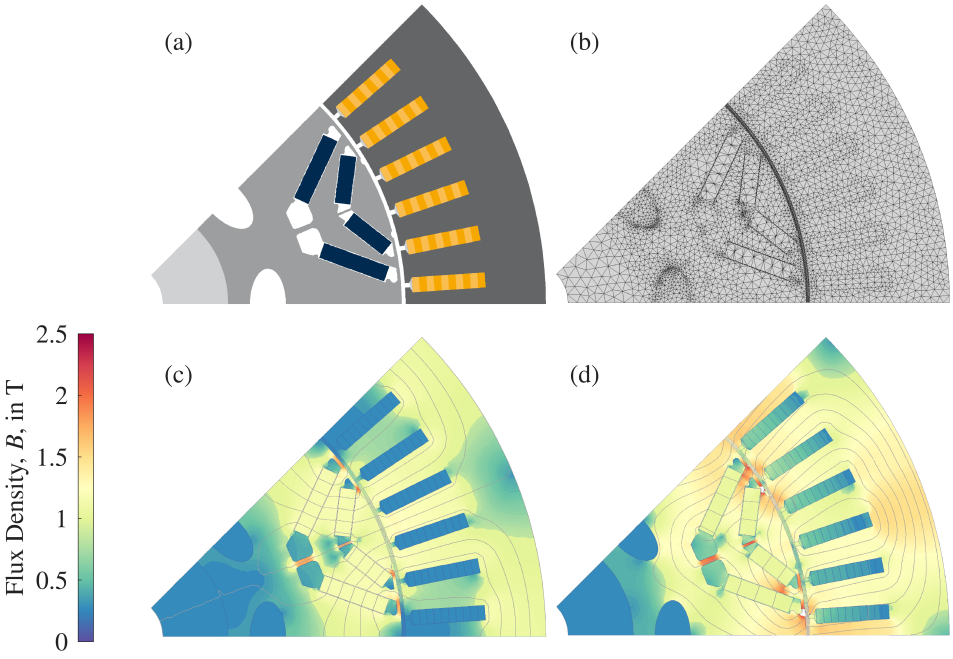


Figure A2. FEA model of machine M3 with (**a**) reconstructed 2D cross-sectional geometry, (**b**) mesh, and (**c**) flux density distribution at open-circuit condition and (**d**) flux density distribution at rated corner-point on-load condition.

Appendix E. FoM Comparison Between Analytical and FEA Models for the Baseline Machines

Table A5. Analytical and FEA figure-of-merit (FoM) comparison for Y–Δ and Y–ΠΙ configurations, machines M1–M6, rounded to two decimal places.

FoM	M1				M2				M3				M4				M5				M6			
	Y–Δ		Y–ΠΙ		Y–Δ		Y–ΠΙ		Y–Δ		Y–ΠΙ		Y–Δ		Y–ΠΙ		Y–Δ		Y–ΠΙ		Y–Δ		Y–ΠΙ	
	Anl.	FEA	Anl.	FEA	Anl.	FEA	Anl.	FEA	Anl.	FEA	Anl.	FEA	Anl.	FEA	Anl.	FEA	Anl.	FEA	Anl.	FEA	Anl.	FEA	Anl.	FEA
$\kappa_{T,c}^{-1}$	2.23	1.83	2.74	2.10	2.17	1.82	2.66	2.17	2.20	1.78	2.71	2.13	2.40	1.58	2.99	1.95	2.60	1.83	3.31	2.15	2.70	1.74	3.47	2.09
$\kappa_{P,\max}$	1.11	1.08	1.11	1.09	1.07	1.06	1.07	1.07	1.11	1.09	1.11	1.10	1.30	1.38	1.38	1.36	1.19	1.28	1.25	1.35	1.14	1.29	1.19	1.35
$\hat{\omega}_{x,1}$	3.09	2.08	3.64	2.32	3.10	2.23	3.64	2.61	3.05	2.13	3.60	2.50	2.34	1.49	2.77	1.69	2.33	1.60	2.74	1.73	2.26	1.50	2.65	1.65
$\kappa_{u,x,1}$	1.20	1.15	1.41	1.28	1.32	1.27	1.56	1.49	1.23	1.18	1.44	1.39	0.51	0.55	0.61	0.63	0.31	0.37	0.37	0.40	0.22	0.26	0.25	0.28
$\kappa_{\mathrm{CPSR,env}}$	1.00	1.01	1.00	1.01	1.00	1.00	1.00	1.00	1.00	1.00	1.00	1.00	2.77	2.51	2.77	2.51	3.16	2.90	3.16	2.90	3.47	3.30	3.47	3.30
$\kappa_{T,\mathrm{env}}$	1.05	1.06	1.04	1.05	1.03	1.03	1.03	1.03	1.05	1.07	1.04	1.06	1.39	1.37	1.34	1.29	1.49	1.46	1.43	1.44	1.58	1.65	1.54	1.66
$\bar{\kappa}_{PF}$	0.06	−0.11	0.12	0.04	0.07	−0.13	0.13	−0.13	0.06	−0.14	0.12	−0.15	0.01	0.04	0.05	0.03	−0.03	−0.03	0.01	−0.04	−0.03	−0.01	−0.01	−0.01
$\bar{\kappa}_{Cu}$	0.11	0.19	0.12	0.25	0.13	0.26	0.14	0.27	0.12	0.23	0.12	0.26	0.02	0.06	0.02	0.03	0.02	0.00	0.01	0.01	0.01	0.00	0.01	0.01

https://doi.org/10.3390/en19204849

Table A6. Error between analytical and FEA FoMs for Y–Δ and Y–Π configurations, machines M1–M6, rounded to two decimal places.

FoM	M1		M2		M3		M4		M5		M6	
	Y–Δ	Y–Π	Y–Δ	Y–Π	Y–Δ	Y–Π	Y–Δ	Y–Π	Y–Δ	Y–Π	Y–Δ	Y–Π
$\kappa_{T,c}^{-1}$	0.4	0.64	0.35	0.49	0.42	0.58	0.81	1.04	0.77	1.16	0.95	1.38
$\kappa_{P,\max}$	0.03	0.02	0.01	0	0.02	0.01	−0.08	0.02	−0.09	−0.1	−0.15	−0.16
$\hat{\omega}_{x,1}$	1.01	1.33	0.88	1.04	0.93	1.09	0.86	1.07	0.74	1.01	0.76	0.99
$\kappa_{u,x,1}$	0.05	0.13	0.05	0.07	0.04	0.05	−0.04	−0.02	−0.05	−0.03	−0.04	−0.03
$\kappa_{\text{CPSR,env}}$	−0.01	−0.01	0	0	0	0	0.26	0.26	0.26	0.26	0.16	0.16
$\kappa_{T,\text{env}}$	0	−0.01	0.01	−0.01	−0.01	−0.02	0.03	0.05	0.03	−0.01	−0.07	−0.12
$\bar{\kappa}_{PF}$	0.17	0.08	0.19	0.27	0.2	0.27	−0.03	0.02	0	0.05	−0.02	0.01
$\bar{\kappa}_{Cu}$	−0.07	−0.13	−0.13	−0.13	−0.12	−0.13	−0.04	−0.01	0.01	0	0.01	0

Table A7. Summary of selected metrics between analytical and FEA FoMs for Y–Δ and Y–Π configurations, machines M1–M6, rounded to two decimal places.

FoM	Median of Error	Standard Deviation of Error	r [a]: Y–Δ	r [a]: Y–Π
$\kappa_{T,c}^{-1}$	0.7	0.33	−0.19	−0.15
$\kappa_{P,\max}$	0.01	0.07	0.89	0.86
$\hat{\omega}_{x,1}$	1	0.16	0.99	0.97
$\kappa_{u,x,1}$	0.01	0.06	1	1
$\kappa_{\text{CPSR,env}}$	0.08	0.13	1	1
$\kappa_{T,\text{env}}$	−0.01	0.05	0.99	0.98
$\bar{\kappa}_{PF}$	0.06	0.11	−0.83	−0.42
$\bar{\kappa}_{Cu}$	−0.06	0.06	0.99	1

[a] Pearson correlation coefficient between analytical and FEA FoMs.

References

1. Petrelli, G.; Nuzzo, S.; Zou, T.; Barater, D.; Franceschini, G.; Gerada, C. Review and Future Developments of Wound Field Synchronous Motors in Automotive. In Proceedings of the 2023 IEEE International Conference on Electrical Systems for Aircraft, Railway, Ship Propulsion and Road Vehicles & International Transportation Electrification Conference (ESARS-ITEC), Venice, Italy, 29–31 March 2023; pp. 1–6. [CrossRef]
2. Tokat, A.; Nguyen, D.K. Drive Cycle Comparison of a PMSM and an EESM for a Traction Application Utilizing Modular Stator Manufacturing. In Proceedings of the 2024 International Conference on Electrical Machines (ICEM), Torino, Italy, 1–4 September 2024; pp. 1–7. [CrossRef]
3. Kallur-Krishnamoorthy, R.; Schröder, M.; Rosen, T.; Andert, J. Rare-Earth-Free Electric Machines with Interchangeable Rotors. *MTZ Worldw.* **2025**, *86*, 16–25. [CrossRef]
4. Dilevrano, G.; Ragazzo, P.; Ferrari, S.; Pellegrino, G. Comparative Design of Ferrite- and NdFeB-PMSMs Using the (x,b) Design Plane. In Proceedings of the 2023 IEEE International Electric Machines & Drives Conference (IEMDC), San Francisco, CA, USA, 15–18 May 2023; pp. 1–7. [CrossRef]
5. Nipp, E.; Norberg, E. On the Feasibility of Switched Stator Windings in Permanent Magnet Motors for Traction Drives. In Proceedings of the Proceedings of the 1998 ASME/IEEE Joint Railroad Conference, Philadelphia, PA, USA, 16 April 1998; pp. 33–39. [CrossRef]
6. Swamy, M.; Kume, T.; Maemura, A.; Morimoto, S. Extended High-Speed Operation via Electronic Winding-Change Method for AC Motors. *IEEE Trans. Ind. Appl.* **2006**, *42*, 742–752. [CrossRef]
7. Nair, S.V.; Layek, K.; Hatua, K. An Unequal Split Dual Three-Phase PMSM With Extended Torque-Speed Characteristics for Automotive Application. *IEEE Trans. Power Electron.* **2022**, *37*, 12437–12449. [CrossRef]
8. Geissler, M.; Osinenko, P.; Herlitzius, T. Winding Switching Strategy for Electric Wheel Drives in Agricultural Machinery. In Proceedings of the 2015 IEEE International Conference on Industrial Technology (ICIT), Seville, Spain, 17–19 March 2015; pp. 851–856. [CrossRef]
9. Cha, K.S.; Park, G.H.; Park, M.R.; Jung, Y.H. Application of Electric Transmission Using Winding Changeover for Performance Improvement of Multilayer Ipmsm Using Ferrite PM. In Proceedings of the 2025 Energy Conversion Congress & Expo Europe (ECCE Europe), Birmingham, UK, 1–4 September 2025; pp. 1–6. [CrossRef]
10. Fuchs, E.; Schraud, J.; Fuchs, F. Analysis of Critical-Speed Increase of Induction Machines via Winding Reconfiguration with Solid-State Switches. *IEEE Trans. Energy Convers.* **2008**, *23*, 774–780. [CrossRef]

11. Scharfenstein, D.; De Doncker, R.W. Extended Operating Range of Induction Machines Using Switched Stator Windings. In Proceedings of the 2019 IEEE International Electric Machines & Drives Conference (IEMDC), San Diego, CA, USA, 12–15 May 2019; pp. 97–103. [CrossRef]
12. Dajaku, G.; Gerling, D. Low Costs and High Efficiency Asynchronous Machine with Stator Cage Winding. In Proceedings of the 2014 IEEE International Electric Vehicle Conference (IEVC), Florence, Italy, 17–19 December 2014; pp. 1–6. [CrossRef]
13. Scharfenstein, D.; Schuller, S.; Quabeck, S.; Doncker, R.W.D. Modeling of Induction Machines with Switched Stator Windings. In Proceedings of the 2020 IEEE Transportation Electrification Conference & Expo (ITEC), Chicago, IL, USA, 23–26 June 2020; pp. 1050–1055. [CrossRef]
14. Tang, L.; Burress, T.; Pries, J. A Reconfigurable-Winding System for Electric Vehicle Drive Applications. In Proceedings of the 2017 IEEE Transportation Electrification Conference and Expo (ITEC), Chicago, IL, USA, 22–24 June 2017; pp. 656–661. [CrossRef]
15. Lee, C.H.; Shin, H.S.; Noh, H.R.; Kim, K.C. A Study on The Electromagnetic Multi-Step Transmission Characteristics of Interior Permanent Magnet Synchronous Motors. *Energies* **2022**, *15*, 9615. [CrossRef]
16. Nipp, E. Permanent Magnet Motor Drives with Switched Stator Windings. Ph.D. Thesis, KTH Royal Institute of Technology, Stockholm, Sweden, 1999.
17. Copt, F.; Araujo, D.M.; Koechli, C.; Perriard, Y. Current Control Strategy for Dynamic Winding Reconfiguration of Slotless Brushless DC Motors. *IEEE Trans. Ind. Appl.* **2019**, *55*, 417–425. [CrossRef]
18. Guo, Q.; Zhang, X.; Liu, Y.; Yang, L.; Cai, W.; Zhang, C.; Zhang, C. Transient Control of Winding Reconfiguration for PMSMs Based on Deadbeat Predictive Control and Zero-Vector Switching. *Electronics* **2026**, *15*, 3120. [CrossRef]
19. Oestreicher, R.; Schneider, J.; Von Ohlen, D.; Fuchs, P.; Kulzer, A.C. Design and Prototyping of a Winding Reconfiguration System for Electric Traction Applications. In Proceedings of the 2026 Stuttgart International Symposium, Stuttgart, Germany, 8 July 2026. [CrossRef]
20. Best, J.; Asef, P.; Vagg, C. A Review of Motors with Reconfigurable Windings for Automotive Traction Drives. *IEEE Access* **2025**, *13*, 140187–140204. [CrossRef]
21. Oestreicher, R.; Koenen, C.; Kulzer, A.C. Analysis of Factors Influencing the Efficiency Improvement Potential of a Winding Changeover in an Electric Machine. *SAE Int. J. Adv. Curr. Pract. Mobil.* **2026**, *8*, 1035–1041. [CrossRef]
22. Clauer, M.; Bauer, D.; Parspour, N. High-Speed Oil-Cooled PMSM with Novel Permanent Magnet Shape and Carbon Fiber Sleeved Rotor for High-Performance Powertrain. *e+i Elektrotech. Inftech.* **2025**, *142*, 114–141. [CrossRef]
23. Wellmann, C.; Khaleel, A.R.; Brinkmann, T.; Wahl, A.; Monissen, C.; Eisenbarth, M.; Andert, J. Electric Machine Co-Optimization for EV Drive Technology Development: Integrating Bayesian Optimization and Nonlinear Model Predictive Control. *eTransportation* **2025**, *23*, 100392. [CrossRef]
24. Wellmann, C.; Rahkola, P.; Tota, S.S.; Pihlatie, M.; Khaleel, A.R.; Marx, C.; Sharma, A.; Eisenbarth, M.; Andert, J. Machine-Learning Integrated Multi-Domain Co-Optimization for Electrified Heavy Duty Fleets. *eTransportation* **2026**, *27*, 100511. [CrossRef]
25. Soong, W.; Miller, T. Theoretical Limitations to the Field-Weakening Performance of the Five Classes of Brushless Synchronous AC Motor Drive. In Proceedings of the International Conference on Electrical Machines and Drives 1993, Oxford, UK, 8–10 September 1993; pp. 127–132.
26. Soong, W.; Miller, T. Field-Weakening Performance of Brushless Synchronous AC Motor Drives. *IEE Proc. Electr. Power Appl.* **1994**, *141*, 331–340. [CrossRef]
27. Jansson, E.; Grunditz, E.; Thiringer, T. Impact of Saturation and Scaling on the Field Weakening Performance of an Interior PM Machine. In Proceedings of the 2020 International Conference on Electrical Machines (ICEM), Gothenburg, Sweden, 23–26 August 2020; pp. 1136–1142. [CrossRef]
28. Hao, L.; Namuduri, C.; Naik, S.M.; Freitas, C. High Speed Performance of PM Machine with Reconfigurable Winding. In Proceedings of the 2015 IEEE Energy Conversion Congress and Exposition (ECCE), Montreal, QC, Canada, 20–24 September 2015; pp. 1840–1848. [CrossRef]
29. Boxriker, M.; Winzer, P.; Kolb, J.; Doppelbauer, M. Increasing the Operating Range of Permanent Magnet Synchronous Motors by Switching the Winding Configurations. In Proceedings of the 2016 IEEE 2nd Annual Southern Power Electronics Conference (SPEC), Auckland, New Zealand, 5–8 December 2016; pp. 1–6. [CrossRef]
30. Boxriker, M.; Kolb, J.; Doppelbauer, M. Effects of Coil Configuration Switching, Pole-Changing and Multi-Phase Windings on Permanent Magnet Synchronous Motors. In Proceedings of the IECON 2017—43rd Annual Conference of the IEEE Industrial Electronics Society, Beijing, China, 29 October–1 November 2017; pp. 1925–1932. [CrossRef]
31. Boxriker, M.; Kolb, J.; Doppelbauer, M. Determining the Volume Optimal Parameter Values for Multi-Phase Permanent Magnet Synchronous Motors with Switchable Coil Configuration. In Proceedings of the 2018 20th European Conference on Power Electronics and Applications (EPE'18 ECCE Europe), Riga, Latvia, 17–21 September 2018.
32. Layek, K.; Roy, D.; Hatua, K. A Split-Tapped Interior Permanent Magnet Synchronous Machine Topology for Electric Vehicles Requiring 3-Speed Transmission. *IEEE Trans. Ind. Electron.* **2026**, *73*, 207–218. [CrossRef]

33. Pellegrino, G.; Vagati, A.; Guglielmi, P. Design Tradeoffs Between Constant Power Speed Range, Uncontrolled Generator Operation, and Rated Current of IPM Motor Drives. *IEEE Trans. Ind. Appl.* **2011**, *47*, 1995–2003. [CrossRef]
34. Fatemi, A.; Demerdash, N.A.O.; Ionel, D.M. Design Optimization of IPM Machines for Efficient Operation in Extended Speed Range. In Proceedings of the 2015 IEEE Transportation Electrification Conference and Expo (ITEC), Dearborn, MI, USA, 14–17 June 2015; pp. 1–8. [CrossRef]
35. Vera, L.J.F.C.; Hsieh, M.F. Investigating the Impact of Characteristic Current on IPMSM Efficiency Area in Flux-Weakening Region. *IEEE Trans. Magn.* **2024**, *60*, 1–6. [CrossRef]
36. Ge, H.; Jiang, J.; Ye, J.; Emadi, A. Behavior Study of Permanent Magnet Synchronous Machines Based on a New Normalized Model. *IEEE Trans. Ind. Electron.* **2019**, *66*, 7539–7550. [CrossRef]
37. Chen, T.; Chen, L.; Chai, F. Behavior Modeling and Design of Winding-Switching Permanent Magnet Synchronous Machine System Based on Normalized Model. In Proceedings of the 2023 26th International Conference on Electrical Machines and Systems (ICEMS), Zhuhai, China, 5–8 November 2023; pp. 5228–5232. [CrossRef]
38. Wang, H.; Kallur-Krishnamoorthy, R.; Neuhaus, C.; Andert, J. Integrated DC Boost Charger in Post-800V Architecture with Open-End Winding Machine—Magnetic-Domain Modelling and Torque Analysis. In Proceedings of the 2026 Stuttgart International Symposium, Stuttgart, Germany, 8 July 2026. [CrossRef]
39. Ansys, Inc. Ansys Motor-CAD User Guide Version 2025. Available online: https://ansyshelp.ansys.com/public/account/secured?returnurl=/Views/Secured/MotorCAD/v252/en/Motor-CAD_UG/MotorCAD/topics/motor-cadmanual.html (accessed on 8 September 2026).
40. Fornasiero, E.; Bianchi, N.; Soong, W.L. Analysis of Torque versus Current Capability of Reluctance and Interior PM Machines under Limited Current and Flux-Linkage Operation. In Proceedings of the 2014 IEEE Energy Conversion Congress and Exposition (ECCE), Pittsburgh, PA, USA, 14–18 September 2014; pp. 4162–4169. [CrossRef]
41. Pellegrino, G.; Bianchi, N.; Cupertino, F.; Jahns, T.M.; Soong, W.L. *The Rediscovery of Synchronous Reluctance and Ferrite Permanent Magnet Motors: Tutorial Course Notes*, 1st ed.; SpringerBriefs in Electrical and Computer Engineering; Springer: Cham, Switzerland, 2016. [CrossRef]
42. Reinert, J.; Brockmeyer, A.; De Doncker, R. Calculation of Losses in Ferro- and Ferrimagnetic Materials Based on the Modified Steinmetz Equation. *IEEE Trans. Ind. Appl.* **2001**, *37*, 1055–1061. [CrossRef]
43. Li, J.; Abdallah, T.; Sullivan, C. Improved Calculation of Core Loss with Nonsinusoidal Waveforms. In *Proceedings of the Conference Record of the 2001 IEEE Industry Applications Conference. 36th IAS Annual Meeting (Cat. No.01CH37248), Chicago, IL, USA, 30 September–4 October 2001*; IEEE: New York, NY, USA, 2001; Volume 4, pp. 2203–2210. [CrossRef]
44. Ruoho, S.; Santa-Nokki, T.; Kolehmainen, J.; Arkkio, A. Modeling Magnet Length in 2-D Finite-Element Analysis of Electric Machines. *IEEE Trans. Magn.* **2009**, *45*, 3114–3120. [CrossRef]
45. Volpe, G.; Popescu, M.; Marignetti, F.; Goss, J. AC Winding Losses in Automotive Traction E-Machines: A New Hybrid Calculation Method. In Proceedings of the 2019 IEEE International Electric Machines & Drives Conference (IEMDC), San Diego, CA, USA, 12–15 May 2019; pp. 2115–2119. [CrossRef]
46. Goss, J.; Mellor, P.H.; Wrobel, R.; Staton, D.A.; Popescu, M. The Design of AC Permanent Magnet Motors for Electric Vehicles: A Computationally Efficient Model of the Operational Envelope. In *Proceedings of the 6th IET International Conference on Power Electronics, Machines and Drives (PEMD 2012)*; IET: Stevenage, UK, 2012; pp. 1–6. [CrossRef]
47. Stipetic, S.; Goss, J.; Zarko, D.; Popescu, M. Calculation of Efficiency Maps Using a Scalable Saturated Model of Synchronous Permanent Magnet Machines. *IEEE Trans. Ind. Appl.* **2018**, *54*, 4257–4267. [CrossRef]

Disclaimer/Publisher's Note: The statements, opinions and data contained in all publications are solely those of the individual author(s) and contributor(s) and not of MDPI and/or the editor(s). MDPI and/or the editor(s) disclaim responsibility for any injury to people or property resulting from any ideas, methods, instructions or products referred to in the content.